

CAPILLARY FORCES ON SEDIMENT PARTICLES:  
EXPERIMENTAL MEASUREMENTS AND  
THEORETICAL ESTIMATES



*Ph.D. Dissertation*  
NIRMALYA CHATTERJEE  
WASHINGTON STATE UNIVERSITY

2013



CAPILLARY FORCES ON SEDIMENT PARTICLES:  
EXPERIMENTAL MEASUREMENTS AND  
THEORETICAL ESTIMATES

By

NIRMALYA CHATTERJEE

A dissertation submitted in partial fulfillment of  
the requirements for the degree of

DOCTOR OF PHILOSOPHY

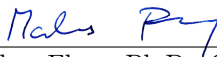
WASHINGTON STATE UNIVERSITY  
Department of Crop and Soil Sciences

AUGUST 2013



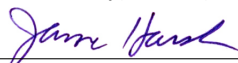
To the Faculty of Washington State University:

The members of the Committee appointed to examine the dissertation of NIRMALYA CHATTERJEE find it satisfactory and recommend that it be accepted.



---

Markus Flury, Ph.D., Chair



---

James B. Harsh, Ph.D.



---

Sergey Lapin, Ph.D.



# Acknowledgements

The road to writing this dissertation has been a long and arduous one. Along the way, many individuals have taken the care and time to teach me the nuances of not just conducting science with all its rigors, but also of navigating life in an academic setting. I take this opportunity to thank all of these individuals who have selflessly given their precious time for both the practice of science and the furtherance of education.

My first thanks are due to my dissertation advisor, Dr. Markus Flury for giving me the opportunity to work with him. I am thankful for his unstinted support and regular pep talks whenever the necessary rigor that good science requires got to me. The things I learnt from him are too numerous to list, but some which needs mention are his approach to addressing scientific problems by keeping the mind open for interdisciplinary work and his admirable ability to be organized, his hard work ethic and his teaching skills. I can undoubtedly say that were he a different person this wouldn't have reached fruition—and would not have been this enriching and fulfilling.

My hearty thanks are also due to the remaining duo in my dissertation committee. Dr. Jim Harsh, whose abiding interest in teaching the underlying basic scientific principles behind the study of a complex system such as soils, and, in the well being of the student are commendable. Dr. Harsh always kept his ears, and, his office door open to my various concerns. My thanks go to Dr. Sergey Lapin for patiently introducing me to a variety of numerical analysis methods and tools to help address my research problems, and for being the sounding board for all the math code that I could come up with. Thanks are also due to Dr. Robert Lewis of WSU Tricities who kindly agreed to work with me, and for supplying important source code so that I didn't need to reinvent the wheel.

My thanks go out to Jeff Boyle and Jon Mathison for helping me familiarize myself to various lab instruments during my first months in Pullman and for getting me started with research at WSU. Thanks are also due to Christine Davitt and Valerie Lynch-Holm for teaching me the use of some of the awesome imaging instruments at the WSU Franceschi Microscopy and Imaging Center and for being there every time I was in the danger of messing up those complex beasts.

I thank my friends, co-workers and fellow graduate students in both Pullman and Puyallup who helped in so many small ways during these past four years, and for just being friends to talk to—their ideas and conversations helped to overcome the obstacles, and their company provided the social life that graduate students often lack. Special thanks for my lab-mates who've become such good friends: Surachet Aramrak, Ziru (Steven) Liu, Thorsten Knappenberger and Prabhakar Singh, and to fellow students Anurag Srivastava, Parama Sikdar, Divya Giri, Mariana Dobre, Rosa Caiazzo, Anna Leon and Kara Lanning—thank you guys for being such great friends. My earnest thanks to Vernene and Lawrence (Larry) Scheurer, for giving me (and Promita) not just a place to stay,

but a home, in Puyallup.

Finally, I would like to thank my family: to my parents for never stopping believing that I had it in me, to my wife, Promita, for her endless love and patience, and lastly, my hearty appreciation for my sister, Nivedita, and brother-in-law, Sitabhra, both academicians themselves for urging me to make this journey—it was as much their journey as it was mine.



# CAPILLARY FORCES ON SEDIMENT PARTICLES: EXPERIMENTAL MEASUREMENTS AND THEORETICAL ESTIMATES

Abstract

by Nirmalya Chatterjee, Ph.D.  
Washington State University  
August 2013

Chair: Markus Flury

At the Hanford Site, radioactive wastes have been disposed into the subsurface. These radionuclides move with infiltrating water both in solution and via adsorption on mobile colloidal soil particles. Extensive research has been directed to understand the mechanism of colloid transport: at field-scale in lysimeters, at laboratory scale in columns and by indirect field measurements. This dissertation investigates experimental and theoretical methods to determine capillary forces on millimeter-scale particles in the subsurface. The specific objectives of this dissertation were:

1. *Measure capillary forces on irregularly shaped sediment particles and compare with theoretical estimates.*

Capillary forces due to a moving air-water interface were measured experimentally on three PTFE particles of standard shape (sphere, circular disc, square tent) and seven natural sediment particles (basalt, granite, hematite, magnetite, mica, milky quartz, quartz) using a tensiometer. Theoretical calculations were done to estimate maximum capillary forces, assuming the particles to be spherical, cylindrical, and ellipsoidal. The ellipsoidal model was found to give the best approximation of the capillary forces.

2. *Measure capillary forces on model particles of standard shapes and compare specific features of the force-position curves with theoretically reconstructed curves.*

Capillary forces due to a moving air-water interface were measured experimentally on nine model polyacrylate particles. Particles were divided

into three categories (rounded, fixed, and tapered) based on cross-section. The theoretical reconstruction of the force-position curves indicated that the pinning, snap-in and snap-off of the air-water interface on sharp edges and variation of cross-section along  $z$ -axis dictated the shape of the force-position curve.

3. *Develop a numerical model to predict capillary forces on subsurface particles.*

Surface roughness features of basalt and quartz sediment particles were reconstructed at triangle resolutions of 3%, 5% and 10% of the particle's root-mean-square radius using scanning electron microscopy. Force-position curves were measured experimentally and calculated theoretically for comparison to determine an optimum mesh resolution. The results provided a lower size-limit of roughness features which can affect capillary forces on mm-scale particles interacting with a moving air-water interface.

# Table of Contents

<b>Acknowledgements</b>	<b>v</b>
<b>Abstract</b>	<b>vii</b>
<b>List of Tables</b>	<b>xiii</b>
<b>List of Figures</b>	<b>xvi</b>
<b>1 Introduction</b>	<b>1</b>
1.1 Background . . . . .	1
1.2 Scope and Objectives . . . . .	3
1.3 Dissertation Outline and Attributions . . . . .	4
<b>2 Capillary Forces between Sediment Particles and an Air-Water Interface</b>	<b>7</b>
2.1 Abstract . . . . .	7
2.2 Introduction . . . . .	8
2.3 Theory . . . . .	9
2.3.1 Forces on a Particle in Contact with an Air-Water Interface	9
2.3.2 Forces on an Ellipsoidal Particle at an Air-Water Interface	10
2.3.3 Forces on a Irregularly-Shaped Particle at an Air-Water Interface . . . . .	10
2.3.4 Dimensionless Variables . . . . .	11
2.4 Materials and Methods . . . . .	11
2.4.1 Particles . . . . .	11
2.4.2 Particle Characterization . . . . .	12
2.4.3 Capillary Force Measurements . . . . .	13
2.5 Data Analysis . . . . .	14
2.6 Results and Discussion . . . . .	14
2.6.1 Interpretation of Force-Position Curves . . . . .	14
2.6.2 Theoretical Maximum Capillary Forces and Pressures . .	15
2.6.3 Experimental Maximum and Snap-off Capillary Forces . . . . .	16

2.6.4	Effect of Solvent Cleaning . . . . .	16
2.6.5	Effect of Hysteresis . . . . .	17
2.6.6	Comparison of Experimental and Theoretical Capillary Forces . . . . .	17
2.7	Implications . . . . .	18
2.8	Tables and Figures . . . . .	18
2.9	Appendix 2A: Supporting Information . . . . .	26
2.9.1	Derivation of Force Balance on an Ellipsoidal Particle at the Air-Water Interface . . . . .	27
2.9.2	Calculating the Undulating Quadrupolar Contact Line on an Ellipsoidal Particle . . . . .	28
2.9.3	Calculation of a Volume-Equivalent Radius and Semi-Major Axes for a Particle . . . . .	29
2.9.4	Errors of Force-Position Measurements . . . . .	30
2.10	Appendix 2B: MatLab Code for Calculating Capillary Rise (Ellipsoidal Particle) . . . . .	42

<b>3</b>	<b>Effect of Particle Shape on Capillary Forces Acting on Particles at the Air-Water Interface</b>	<b>45</b>
3.1	Abstract . . . . .	45
3.2	Introduction . . . . .	46
3.3	Theory . . . . .	48
3.3.1	Capillary Force . . . . .	48
3.3.2	Gibbs' Inequality . . . . .	49
3.4	Experimental Section . . . . .	50
3.4.1	Model Particles . . . . .	50
3.4.2	Capillary Force Measurements . . . . .	51
3.4.3	Surface Characterization with SEM . . . . .	51
3.4.4	High-speed Video Capture of Interface Pinning on Model Particles . . . . .	51
3.4.5	Numerical Calculation of Capillary Forces . . . . .	52
3.5	Results and Discussion . . . . .	52
3.5.1	Results Expected from Theory . . . . .	52
3.5.2	Observations from High-Speed Videos . . . . .	54
3.5.3	Description of Experimentally Obtained Force-Position Curves . . . . .	55
3.5.4	Reconstruction and Interpretation of Force-Position Curves	55
3.5.5	Maximum Capillary Forces and Snap-off Forces . . . . .	57
3.6	Implications . . . . .	57
3.7	Tables and Figures . . . . .	58
3.8	Appendix 3A: Supporting Information . . . . .	68
3.8.1	Method for High-speed Videography . . . . .	69
3.8.2	Discussion . . . . .	69

<b>4</b>	<b>Numerical Simulation of Capillary Forces Acting on Subsurface Particles at Air-Water Interfaces</b>	<b>73</b>
4.1	Abstract . . . . .	73
4.2	Introduction . . . . .	74
4.3	Theory . . . . .	75
4.3.1	Capillary Rise and Total Force on a particle at an Air-Water Interface . . . . .	75
4.3.2	Gibbs' Inequality and Interfacial Pinning . . . . .	76
4.4	Materials and Methods . . . . .	77
4.4.1	Capillary Force Measurements . . . . .	77
4.4.2	Particles . . . . .	77
4.4.3	Surface Characterization by Electron Microscopy . . . . .	77
4.4.4	SEM Image Processing . . . . .	78
4.5	Data Analysis . . . . .	78
4.5.1	Point-Cloud Generation . . . . .	78
4.5.2	Surface Reconstruction by Triangulation of Point-Cloud . . . . .	78
4.5.3	Theoretical Reconstruction of Force Position Curves . . . . .	79
4.6	Results and Discussion . . . . .	80
4.6.1	Analysis and Interpretation of Force-Position Curves . . . . .	80
4.6.2	Comparison of Experimental and Theoretical Capillary Forces . . . . .	80
4.7	Implications . . . . .	81
4.8	Tables and Figures . . . . .	82
<b>5</b>	<b>Summary and Conclusions</b>	<b>91</b>
5.1	Calculating Capillary Forces on Sediment Particles Shaped as Spheres, Ellipsoids and Cylinders. . . . .	91
5.2	Capillary Forces on 3D Printed Particles of Standard Geometric Shapes. . . . .	92
5.3	Numerical Reconstruction of Surfaces and Force-Position Curves of Natural Sediment Particles. . . . .	93
5.4	Conclusion . . . . .	93
	<b>Bibliography</b>	<b>95</b>



# List of Tables

2.1	Maximum capillary forces (experimental and theoretical). . . . .	19
2.2	Particle characterization in terms of spatial dimensions and contact angle with an air-water interface. . . . .	32
2.3	Particle volume, radius of volume-equivalent sphere ( $r_{ve}$ ) and semi-major axes of volume-equivalent ellipsoids (using both maximum $a : b : c$ and root-mean-square (rms) $a : b : c$ ratios). . . . .	33
2.4	Experimental and theoretical maximum forces, percentage increase in contact line due to undulations, and capillary pressures. . . . .	34
2.5	Experimental maximum and snap-off capillary forces for different particles. . . . .	35
3.1	Characteristics of model particles. . . . .	59
3.2	Pinning distances and maximum capillary forces (experimental and theoretical). Negative forces indicate upward forces, that is, forces pointing in direction from the water to the air phase. . . . .	60
4.1	Particle dimensions and contact angles . . . . .	82
4.2	Mesh generation (triangulation) using the Ball Pivot (BP) Algorithm. (Top: input parameters; bottom: results.) . . . . .	83





# List of Figures

1.1	Schematic of solid-air-water contact angle on a (a) smooth and (b) rough surface. . . . .	3
2.1	Forces on an ellipsoid and a rough particle . . . . .	20
2.2	SEM of PTFE and natural sediment particles . . . . .	21
2.3	Labeled force-position curve - complete cycle . . . . .	22
2.4	Force-position curve during immersion - PTFE and natural sediment particles . . . . .	23
2.5	Dimensionless force-position curve . . . . .	24
2.6	Immersion force-position curve of a quartz particle pre- and post-cleaning . . . . .	25
2.7	Schematic of an ellipsoidal particle at an air-water interface . . .	36
2.8	Schematic of calculation steps . . . . .	37
2.9	Dissection scope images . . . . .	38
2.10	Schematic of capillary force measurements with a process tensiometer. . . . .	39
2.11	Force-position curves of wet particles . . . . .	40
2.12	Dimensionless force-position curve for all particles . . . . .	41
2.13	Ellipsoid capillary rise . . . . .	43
3.1	Dissection scope (top) view and 3D render model of the nine particles	61
3.2	Schematic diagram of particle / air-water interface interaction . .	62
3.3	SEM images of 3D printed particle surfaces . . . . .	63
3.4	Schematic of tensionmeter set-up . . . . .	64
3.5	Schematic of immersion force-position curves for three particle categories . . . . .	65
3.6	Typical experimental force-position curve during immersion (ellipsoid) . . . . .	66
3.7	Comparison of experimental and reconstructed, theoretical force-position curves (all 9 model particles) . . . . .	67
3.8	Snap-shots of particles of different cross-sections prior to snap-in of the air-water interface. . . . .	70

3.9	Comparison of experimental and scaled, reconstructed, theoretical force position curves . . . . .	71
4.1	Schematic of force-position curve measurement apparatus (Tensiometer). . . . .	84
4.2	Dissection scope (top) and scanning electron microscope (bottom) images of a basalt (left) and a quartz (right) sediment particle. .	85
4.3	Flow-chart of obtaining 3D mesh from SEM images. . . . .	86
4.4	Comparison of reconstructed surfaces for natural sediment particles (basalt and quartz). . . . .	87
4.5	Polygons of intersection and immersed volumes of mesh for different $z$ -values (both basalt and quartz particles). . . . .	88
4.6	Comparison of experimental and theoretically reconstructed force-position curves for a basalt and a quartz particle. . . . .	89

# Chapter 1

## Introduction

### 1.1 Background

Colloidal soil particles play an important role in subsurface transport of pollutants and contaminants. Previous studies have looked into this aspect of soil colloids for an understanding of its effect on groundwater quality [McCarthy and Zachara, 1989; Kretzschmar *et al.*, 1999]. Results of both laboratory [Grolimund *et al.*, 1996; Karathanasis, 1999; Flury *et al.*, 2002] and field scale [Ryan *et al.*, 1998] experiments have shown evidences of soil-colloid mediated contaminant transport. Soil types, the physical and chemical properties of soils, and the chemistry of the contaminants play a role in the final fate and transport mechanisms of colloids in the soil subsurface [Kretzschmar *et al.*, 1999; McCarthy and McKay, 2004; Flury and Qiu, 2008].

The presence of an air-water interface inside an unsaturated porous media has a major role in colloid transport. Colloidal particles can attach to the stationary air-water interface [Wan *et al.*, 1994; Keller and Auset, 2007] or get attached to three-phase junctions of air-water interfaces [Crist *et al.*, 2004; Crist *et al.*, 2005; Zevi *et al.*, 2005] moving over solid surfaces of particles in porous media like soils or sediments. This causes reduced movement of the colloidal particles in porous media. Water movement through a porous media also causes colloid movement during both infiltration [Jacobsen *et al.*, 1998; Gao *et al.*, 2004; Levin *et al.*, 2006] and drainage [Zhuang *et al.*, 2007; Cheng and Saiers, 2009] events. Colloid attachment to, and subsequent movement with, an air-water interface has been demonstrated with a moving infiltration front in porous media [Sharma *et al.*, 2008b]. Previous studies involving visualization of pore-scale water have also shown colloid attachment and movement at air-water interfaces [Leenaars and O'Brien, 1989; Noordmans *et al.*, 1997; Gomez-Suarez *et al.*, 1999b; Gomez-Suarez *et al.*, 1999a; Sharma *et al.*, 2008b]. The above studies indicate that air-water and air-water-solid interfaces and their movement constitute an important mobilization and transport mechanism for colloids.

A particle attached to an air-water interface experiences forces due to surface tension of the interface as well as due to pressure differences at the interface. In porous media, these forces cause the particle to experience a strong force which cause it to pin down to solid surfaces, especially in conditions of low water saturation [Wan and Tokunaga, 1997; Shang et al., 2008; Gao et al., 2008]. As water saturation levels increases the thickness of the water film in porous media increases and the particle on a solid surface tends to remain attached to the air-water interface [Wan and Tokunaga, 1997; Veerapaneni et al., 2000]. The pinning force eventually disappears allowing detachment of the particle from the solid surface [Shang et al., 2008; Shang et al., 2009]. There is also confirmation from theoretical calculations that capillary forces can exceed DLVO forces (electrical double layers and van der Waals forces) [Scheludko et al., 1976; Preuss and Butt, 1998b; Shang et al., 2008; Sharma et al., 2008b].

Tensiometry is a method which has been extensively used for more than a century to measure surface and interfacial tension [Zhang et al., 1996; Zhang et al., 1997]. Sphere tensiometry is a proposed method of using a standardized spherical particle to measure interfacial forces, as an alternative to more widespread and older methods, like the Wilhelmy plate or du Noüy ring methods [Gunde et al., 1995; Ecke et al., 1999]. In the past couple of decades, surface microscopic methods like atomic force microscopy have also been used to measure interfacial forces on colloidal-sized particles [Preuss and Butt, 1998a; Preuss and Butt, 1998b; Gillies et al., 2005; Englert et al., 2009; Yamamoto et al., 2010]. In almost all these experiments the particle shape has been kept standardized to a sphere, ring or plate to ease calculations.

Numerical solutions of the Young-Laplace equation using boundary conditions for a spherical particle have been used [Princen, 1969; Zhang et al., 1996; Zhang et al., 1997; Zhang et al., 1999] and have been found to agree well with experimental data [Zhang et al., 1996; Zhang et al., 1997; Shang et al., 2009]. Numerical solutions on symmetric but non-spherical particles, like those with edges like right cylinders [Hesla and Joseph, 2004; Singh and Joseph, 2005], cubes or pyramidal shapes, become more complicated due to additional boundary conditions that need to be considered. No numerical solutions have been reported for irregularly-shaped particles. Recent work by Morris et al. [2011] have focused on using a class of equations called ‘superquadrics’ to mathematically model regular geometric shapes like spheres, cylinders, ellipsoids, tent- and pyramidal shapes using a single parametrized equation. The particle edges in these studies [Morris et al., 2008; Morris et al., 2010; Morris et al., 2011] are, however, theoretically very tightly curved surfaces and the flat surfaces are ‘smooth’ surfaces, and hence do not model real rough or sharply-edged particles. These studies used a finite-element method to model the surface energy maps of the particles.

The shape and surface properties of the particle determine the orientation of the air-water interface meniscus. For smooth surfaces, the contact angle con-

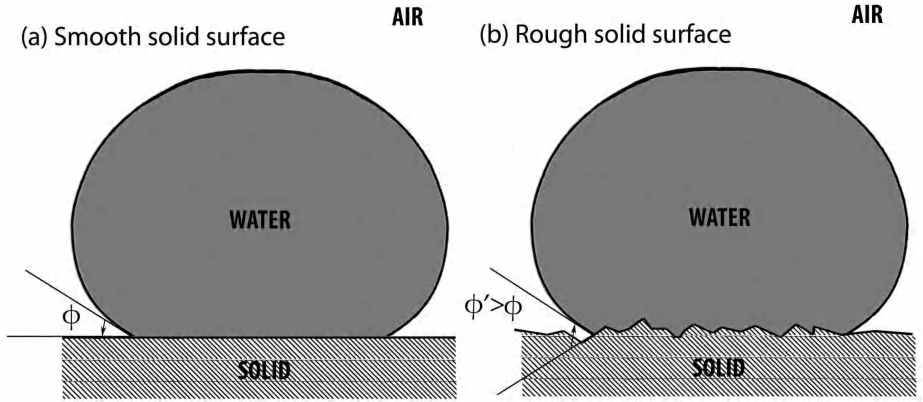


Figure 1.1: Schematic of solid-air-water contact angle on a (a) smooth and (b) rough surface.

controls the boundary condition at the contact line (Figure 1.1a), whereas for rough surfaces, both surface roughness and contact angle determine the boundary condition (Figure 1.1b). To calculate the exact shape of the air-water interface for irregular particles, knowledge of the surface roughness is needed. The scale and degree of the roughness affects the magnitude of the capillary force and also determines how the interface slips and moves across the solid surface, i.e., whether the interface slips or jumps, and where it jumps. No-slip conditions arise due to surface roughness conditions, where the air-water interface is temporarily being pinned [Hesla and Joseph, 2004; Singh and Joseph, 2005].

## 1.2 Scope and Objectives

The overall goal of this dissertation is to advance our understanding of how colloids move in unsaturated porous media like soils and sediments. We want to understand the effects of air-water interfaces on fate and transport of colloids in the sub-surface. The specific objectives were (1) to quantify, both experimentally and theoretically, the capillary forces acting on natural sub-surface particles at an air-water interface, (2) elucidate the effect of particle shape on capillary forces, and (3) to develop a mathematical model to predict capillary forces for irregularly-shaped particles.

The studies were undertaken with millimeter-scale particles. The experimental capillary force measurements were done using a process tensiometer. The capillary forces measured were of the order of micro- to milli-newtons. The par-

ticles that were used in these studies were either natural sediment particles from the deep vadose zone of the US DOE Hanford Site, or synthetically manufactured particles using three-dimensional printing processes.

## 1.3 Dissertation Outline and Attributions

This dissertation consists of five (5) chapters.

1. Chapter 1 (this chapter) gives a brief background on capillary forces and its importance in the fate and transport of nutrients and contaminants in porous media and in the soil subsurface. It also describes the scope and objectives of this dissertation.

2. Chapter 2 was published as a journal article: Chatterjee, N., S. Lapin, and M. Flury, (2012), Capillary forces between sediment particles and an air-water interface, *Environ. Sci. Technol.*, 46, 4411–4418.

This chapter focuses on developing a mathematical model to calculate capillary force on irregular particles, assuming them to be triaxial ellipsoids. A comparison of the theoretically calculated forces with experimentally measured ones is done to test the efficacy of the model.

The paper was written in the most part by me with considerable editing and content addition by Dr. Flury. Dr. Lapin helped in testing the Matlab code, checked the math for the ellipsoidal model, and provided technical, editorial and scientific inputs. Dr. Harsh provided suggestions during numerous group meetings.

3. Chapter 3 has been submitted for review to the journal *Langmuir*: Chatterjee, N., and M. Flury, (2013), Effect of particle shape on capillary forces acting on particles at the air-water interface.

The paper was written in the most part by me with considerable editing and content addition by Dr. Flury. Dr. Harsh provided suggestions during numerous group meetings.

Special thanks are due to Surachet Aramrak for taking the SEM images of the model particles and to Thorsten Knappenberger for suggesting the use of 3D printing technology to generate the model particles and for arranging for the loan and transport of the high-speed video camera from the University of Hohenheim, Germany.

4. Chapter 4 is intended to be submitted as a journal article. The basic objective of the chapter is to find the effect of resolution of reconstructed meshes on the features observed in theoretical force-position curves. The studies were made to model the surface roughness of mm-scale particles, using scanning electron microscopy.

This chapter was mostly written by me with editorial and scientific inputs from Dr. Flury, Dr. Lapin and Dr. Harsh. Dr. Robert Lewis (Dept. of

Electrical Engineering & Computer Science, WSU Tricities) very graciously provided the Python code to output areas of polygons of intersection from a supplied PLY file; he also helped with the numerical aspects of the simulations.

5. Chapter 5 summarizes the results and discusses the implications of the investigations described in Chapters 2–4 in colloid and colloid-mediated contaminant transport in porous media and in the soil subsurface.





# Chapter 2

## Capillary Forces between Sediment Particles and an Air-Water Interface

### 2.1 Abstract

In the vadose zone, air-water interfaces play an important role in particle fate and transport, as particles can attach to the air-water interfaces by action of capillary forces. This attachment can either retard or enhance the movement of particles, depending on whether the air-water interfaces are stationary or mobile. Here we use three standard PTFE particles (sphere, circular cylinder, and tent) and seven natural mineral particles (basalt, granite, hematite, magnetite, mica, milky quartz, and clear quartz) to quantify the capillary forces between an air-water interface and the different particles. Capillary forces were determined experimentally using tensiometry, and theoretically assuming volume-equivalent spherical, ellipsoidal, and circular cylinder shapes. We experimentally distinguished between the maximum capillary force and the snap-off force when the air-water interface detaches from the particle. Theoretical and experimental values of capillary forces were of similar order of magnitude. The sphere gave the smallest theoretical capillary force, and the circular cylinder had the largest force due to pinning of the air-water interface. Pinning was less pronounced for natural particles when compared to the circular cylinder. Ellipsoids gave the best agreement with measured forces, suggesting that this shape can provide a reasonable estimation of capillary forces for many natural particles.

---

This chapter was published as a journal article: Chatterjee, N., S. Lapin, and M. Flury, (2012), Capillary forces between sediment particles and an air-water interface, *Environ. Sci. Technol.*, **46**, 4411–4418.

## 2.2 Introduction

Soil particles in the colloidal fraction are relevant for their role in facilitation of subsurface contaminant transport [Kretzschmar *et al.*, 1999; McCarthy and Zachara, 1989]. In unsaturated porous media, such as vadose zone sediments, the presence of the air-water interface plays an important role on fate and transport of colloids. Colloids can attach to stationary air-water interfaces in porous media [Keller and Auset, 2007; Wan *et al.*, 1994]. It has been observed that colloids can be mobilized during infiltration [Gao *et al.*, 2004; Jacobsen *et al.*, 1998; Levin *et al.*, 2006; Shang *et al.*, 2008] and drainage [Cheng and Saiers, 2009; Zhuang *et al.*, 2007] events. Sharma *et al.* [2008a] demonstrated that colloids attach and move along with air-water interfaces such as an infiltration front through a porous medium. Mechanistic studies involving pore-scale visualization confirm that colloids can be captured at the air-water interface and carried along with the moving air-water interface [Aramrak *et al.*, 2011; Gomez-Suarez *et al.*, 1999b; Gomez-Suarez *et al.*, 1999a; Leenaars and O'Brien, 1989; Noordmans *et al.*, 1997; Sharma *et al.*, 2008b].

When a particle is attached to an air-water interface the particle experiences forces both due to surface tension and pressure differences. In a porous medium, these forces can cause a strong attraction of a particle to the stationary solid surfaces when the water saturation is low, and air-water interfaces pin the particles to solid surfaces [Shang *et al.*, 2008; Gao *et al.*, 2008; Wan and Tokunaga, 1997]. As water saturation increases and liquid films become thicker, this particle pinning disappears [Wan and Tokunaga, 1997; Veerapaneni *et al.*, 2000], and particles are even subject to a repulsive force that can lead to particle detachment from the solid surface [Shang *et al.*, 2008; Shang *et al.*, 2009]. Theoretical calculations confirm that capillary forces can exceed DLVO forces [Shang *et al.*, 2008; Sharma *et al.*, 2008b; Preuss and Butt, 1998b; Scheludko *et al.*, 1976].

Macroscopic techniques like tensiometry have been used to directly measure the capillary forces between a spherical particle and the air-water interface [Zhang *et al.*, 1996; Zhang *et al.*, 1997]. More recently, microscopic techniques like atomic force microscopy have been used to measure capillary forces for colloidal sized-particles [Preuss and Butt, 1998b; Preuss and Butt, 1998a; Gillies *et al.*, 2005; Englert *et al.*, 2009; Yamamoto *et al.*, 2010]. In these experiments, the measurements are usually done with spherical particles. Sphere tensiometry (i.e., using a sphere for tensiometric force measurements) has even been proposed as an alternative method to the de Noüy ring and Wilhelmy plate methods for measuring surface tensions and contact angles [Gunde *et al.*, 1995; Ecke *et al.*, 1999].

Capillary forces acting on a spherical particle can be calculated from theory using numerical solutions of the Young-Laplace equation [Zhang *et al.*, 1996; Zhang *et al.*, 1997; Princen, 1969; Zhang *et al.*, 1999]. For particles with non-spherical but regular shapes, especially those with sharp edges the numerical solution becomes more complicated due to additional boundary conditions that

need to be applied [Hesla and Joseph, 2004; Singh and Joseph, 2005]. The shape and surface properties of the particle determine the orientation of the air-water interface meniscus. The scale and degree of the roughness affects the magnitude of the capillary force and also determines how the interface moves across the solid surface, i.e., whether the interface slips or jumps, and where it jumps. No-slip conditions arise due to surface roughness conditions, where the air-water interface is temporarily being pinned [Hesla and Joseph, 2004; Singh and Joseph, 2005].

In previous experiments [Shang *et al.*, 2009], our group has quantified capillary forces on regularly-shaped particles (spheres, cylinders, cubes) using tensiometry, and we have also made some force measurements on natural subsurface particles. Here, we expand upon those previous measurements, by focusing on natural subsurface particles and by quantifying the effects of particle shape and roughness. We further investigate the effect of natural surface coatings on the magnitude of the capillary force.

## 2.3 Theory

### 2.3.1 Forces on a Particle in Contact with an Air-Water Interface

Figure 2.1 shows a schematic of an ellipsoidal and an irregularly-shaped particle attached to a solid surface and in contact with an air-water interface. The theory presented here follows the discussion presented in Zhang *et al.* [Zhang *et al.*, 1996]. We consider that the solid surface is horizontal and that the air-water interface at  $x \rightarrow \infty$  is also horizontal. The forces acting on the particle in a static system are (1) the DLVO force ( $f_{\text{DLVO}}$ ), the (2) the gravity force ( $f_w$ ), the (3) surface tension force ( $f_s$ ), the (4) buoyancy force ( $f_b$ ), and the (5) hydrostatic pressure force ( $f_p$ ). The force balance on the particle is then given as [Shang *et al.*, 2009]:

$$f = f_{\text{DLVO}} + f_w + f_s + f_b + f_p \quad (2.1)$$

The sum of the surface tension ( $f_s$ ) and hydrostatic pressure ( $f_p$ ) forces is also known as the capillary force. If the particle is symmetric, the force balance  $f$  is parallel to the  $z$ -direction (Figure 2.1a), but if the particle is asymmetric (Figure 2.1b), the directions of  $f_s$  and  $f_p$  forces are determined by the contact angle of the air-water interface at the particle surface. Further, for asymmetric particles, the interface line is undulating in quadrupolar fashion [Brown *et al.*, 2000; Stamou *et al.*, 2000; Fournier and Galatola, 2002; Danov *et al.*, 2005; van Nierop *et al.*, 2005; Lehle *et al.*, 2008]. If  $f < 0$  the particle will be detached from the solid surface, if  $f > 0$  the particle will remain pinned to the solid surface.

### 2.3.2 Forces on an Ellipsoidal Particle at an Air-Water Interface

Here, we extend the theory for a spherical particle to a triaxial ellipsoid. Theoretical calculations [Brown *et al.*, 2000; Stamou *et al.*, 2000; Fournier and Galatola, 2002; Tee, 2004; Danov *et al.*, 2005; van Nierop *et al.*, 2005; Lehle *et al.*, 2008; Danov and Kralchevsky, 2010] of capillary forces on ellipsoidal particles showed that the contact line is of an undulating, elliptic shape rather than a flat ellipse. We calculated the length of the undulating contact line following the approach of van Nierop *et al.* [van Nierop *et al.*, 2005] (see supporting information for details). The force balance on an ellipsoidal particle is then given as:

$$\begin{aligned} f = & 4a\kappa E(e_{xy})\gamma \cos \beta \sin \phi_c \\ & + \pi ab\Delta\rho g z_c \cos^2 \beta \\ & - \frac{\pi}{3}\Delta\rho g abc(2 + 3 \sin \beta - \sin^3 \beta) \end{aligned} \quad (2.2)$$

where  $a$ ,  $b$ , and  $c$  are the semi-principal axes of the ellipsoid along the three coordinate axes  $x$ ,  $y$ , and  $z$ , respectively,  $\kappa$  is the ratio representing increase in contact line due to undulation,  $E(e_{xy})$  is the complete elliptic integral of the second kind with eccentricity  $e_{xy}$ ,  $\beta$  is the parametric latitude (Figure 2.7, supporting information),  $\gamma$  is the surface tension of water,  $\phi_c$  is the angle of inclination of the undistorted air-water interface at the three-phase contact line,  $\Delta\rho = (\rho_l - \rho_g)$  is the difference between the two fluid densities  $\rho_l$  (water) and  $\rho_g$  (air),  $g$  is the acceleration due to gravity, and  $z_c$  is the deflection depth (position of the average contact line on the  $z$ -axis).

### 2.3.3 Forces on a Irregularly-Shaped Particle at an Air-Water Interface

The movement of the air-water interface (the macroscopic interface) on a solid surface is dependent on the geometry and the surface properties of the solid surface. In the case of ideally smooth surfaces, the air-water interface intersects the solid surface at an angle and a position determined by the capillary forces and the equilibrium air-water-solid contact angle.

In a dynamic system, where the air-water interface moves over a particle, surface roughness can cause the air-water interface to be pinned at surface discontinuities. While for a smooth particle, the air-water-solid interface line adjusts its position to the respective equilibrium position (Figure 2.1a), the pinning at surface discontinuities for rough particles causes the air-water interface to exceed its equilibrium configuration (Figure 2.1b). The increase in the contact angle can mathematically be formulated by the Gibbs extension of the Young

Equation [Singh and Joseph, 2005]:

$$\theta_0 < \theta < 180^\circ - \alpha + \theta_0 \quad (2.3)$$

where  $\alpha$  is the wedge angle and  $\theta_0$  is the equilibrium contact angle for the vertical face (Figure 2.1b). The pinning causes the air-water interface to distort. These distortions cause large forces on the air-water interfaces, which tend to give way suddenly when the interface is moved beyond a critical distance, causing the contact line to snap off.

The approximation of a natural particle as a right, circular cylinder takes into consideration the maximum force due to the condition described by Eq. 4.3. The equation for the force balance on a right, circular cylinder [Shang et al., 2009] is:

$$f = -2\pi r \gamma \sin(\theta - \pi/2) - \Delta\rho g(z_0 + L)\pi r^2 \quad (2.4)$$

where  $L$  is the length of the cylinder.

### 2.3.4 Dimensionless Variables

The distances and forces can be represented in dimensionless form [Zhang et al., 1996] as follows (capital letters represent dimensionless variables):

$$X = x\sqrt{c_a} \quad \text{and} \quad Z = z\sqrt{c_a} \quad \text{and} \quad R = r\sqrt{c_a} \quad \text{and} \quad H = h\sqrt{c_a} \quad (2.5)$$

$$R_X = r_x\sqrt{c_a} \quad \text{and} \quad R_Y = r_y\sqrt{c_a} \quad \text{and} \quad R_Z = r_z\sqrt{c_a} \quad (2.6)$$

where  $x, y$  and  $z$  are the directions parallel and perpendicular to the undisturbed air-water interface,  $r$  is the radius of the particle measured from the  $z$ -axis,  $h$  is the distance of the base of the particle from the undisturbed interface, and  $c_a$  is the capillary constant ( $c_a = \Delta\rho g/\gamma$ ), where  $\Delta\rho$  is the density differences between the liquid and the gas, and  $\gamma$  is the surface tension. The dimensionless capillary force  $F$  is given as:

$$F = \frac{f}{r^3 \Delta\rho g} \quad (2.7)$$

where  $f$  is the dimensional force.

## 2.4 Materials and Methods

### 2.4.1 Particles

We used three particles of well-defined, standard shape and several natural sediment particles. The standard particles were made of PTFE and consisted of a sphere, a cylindrical disk, and a tent. The natural sediment particles came from the Hanford formation at the US Nuclear Hanford Reservation in south-central Washington. The sediments were collected from 20 m depth below surface

from a trench face at the Hanford Environmental Restoration Disposal Facility. The sediments were air-dried and sieved through meshes with nominal sizes 1 mm and 2 mm; the fraction between 1 and 2 mm was collected. We placed these sediments then under a dissection scope and picked individual particles with tweezers. We selected particles with typical mineralogy for the Hanford sediments: basalt, granite, hematite, magnetite, mica, milky quartz, and clear quartz. Three particles for each type of particle were selected and stored in 20 mL glass vials. Figure 2.9 (supporting information) shows photographic images of the particles.

Individual sediment particles were mounted on J-shaped hooks made of steel wires with diameter of 0.5 mm (Figure 2.10, supporting information). The lower end of the hooks were flattened with a file, and the hooks were cleaned by rinsing successively with acetone, ethanol, and deionized water. Particles were then attached to the hooks with instant glue (Dr. Bond SuperGlue, ITW Inc., Solon, OH). The lower end of the hook was attached to the bottom of the particle so that it did not interfere with the movement of the interface when it approaches the particle surface from the top. Particles were always handled with clean tweezers to avoid surface contamination.

## 2.4.2 Particle Characterization

Particles were characterized for air-water contact angles, shape, and surface roughness. The air-water-solid contact angle was determined using a goniometer (CA Goniometer Model 50-00-115, Ramé-Hart Instrument Co., Netcong, NJ). The PTFE particles and the natural particles as obtained were mounted on a microscopy slide using double-sided tape. A micro-syringe (steel needle with 0.5 mm o.d.) was used to put a drop of water (25  $\mu$ L) centered 0.3 mm away from the edge of the particle, so that the particle touched the side of the drop.

For electron microscopic characterizations, the particles were coated with platinum-palladium to a thickness of 3 nm under a sputter coater (Model 108auto, Cressington Scientific, Watford, England). The particles were then examined under an environmental scanning electron microscope (SEM) equipped with a field emission electron gun (FEI Quanta 200F, FEI Co., Hillsboro, OR). The particles were kept oriented under the SEM in the same manner as for the force-position and contact angle measurements. If observed directly from above, this gives the  $xy$ -plane view of the particle. Additional images were taken at a  $90^\circ$  view ( $xz$ -plane) to determine the overall cross-section of the particle. Particle dimensions were measured with the SEM measuring software. The SEM analysis was done after the contact angle and capillary force measurements (see below), because the surface properties were irreversibly altered by the sputter coating.

The particle outlines under the SEM in the  $xy$ - and  $xz$ -planes were used to determine the dimensions along the three coordinate axes. Figure 2.2 shows SEM images perpendicular to the  $xy$ -plane. We further calculated a root mean square value of the coordinates  $x, y, z$ , as well as a volume-equivalent spherical radius

and ellipsoidal semi-major axes for each particle (see supporting information for details on calculations and Tables 2.2 and 2.3 for summary of data).

### 2.4.3 Capillary Force Measurements

The capillary forces between the particles and the air-water interface were measured with a tensiometer (Process Tensiometer K100, Krüss GmbH, Hamburg, Germany). The precision of the tensiometer microbalance is 0.02 mg corresponding to a force of 0.196  $\mu\text{N}$ . The J-shaped steel hook with the particle attached was fastened to the microbalance of the tensiometer (Figure 2.10, supporting information). A glass cup (inner diameter 65.7 mm, height 37.9 mm) was filled with deionized water (electrical conductivity of 5.5  $\mu\text{S m}^{-1}$ ) and placed into the temperature jacket of the tensiometer (kept at 23°C).

The particle and the hook were initially in the air phase. The particle on the hook was kept stationary, while the air-water interface, formed in the glass cup below, was moved upwards at a constant velocity of 1.0 mm min<sup>-1</sup>, so that it approached the particle from the bottom (Figure 2.10, supporting information). The interface made contact with the bottom part of the steel hook first, before wetting the particle itself. The tensiometer measured the force exerted on the microbalance after every position increment of 0.05 mm. These measurements were continued until the entire particle was completely immersed in water and the air-water interface had detached from the particle and passed to a position above the particle. The air-water interface was then lowered at the same velocity until the particle came back to its initial position above the interface in the air phase. By plotting force versus position, we obtained the so-called force-position curves.

Each particle was measured in a specific sequence of immersion and washing. First, the particle under air-dry conditions was mounted onto the tensiometer and immersed into the water to measure a force-position curve. This represents an initially dry particle, taken “as is” from the sediments, with its surface not modified by wetting or washing. Then, the particle was again immersed into the water, for five repeated cycles without allowing it to dry. These measurements represent force-position curves for an initially wet particle. After this sequence the particle was washed with acetone and ethanol, and then air-dried for five minutes. The solvent rinsing was performed to remove soluble organic matter coatings on the particle surface. This cycle (one measurement for the air-dry particle and five for the wet particle) of immersion-emersion mentioned above was repeated with the cleaned particle. The data were then used to construct force-position curves for (1) dry, (2) wet, (3) cleaned-dry, and (4) cleaned-wet particles. The replicated runs for the wet (non-cleaned and cleaned) particles were averaged and used to calculate error bars (standard deviations) for the force-position curves, and to determine the measurement precision.

For each particle, we used the same water in the glass cup, but we changed the water for every new particle. Surface tension of the water was measured

before and after each force-position curve with the Wilhelmy plate method. The errors in force measurements are discussed in the supporting information.

## 2.5 Data Analysis

The force position curves were analyzed to determine the forces exerted on the particle by the moving air-water interface. We were particularly interested in the maximum detachment forces as well as the snap-off forces. The maximum detachment force is defined at the maximum force recorded by the tensiometer in upward vertical direction, whereas the snap-off force is the force recorded when the air-water interface snaps off from the solid surface. The snap-off force was observed from the force-distance curve when the measured force decreased markedly within a short distance increment, which we found by computing the first derivative of the force-distance curve. The position where the change in force with change in position is maximal is the point of snap off.

We used the theory for a sphere (Eq. 2.12), a circular cylinder (Eq. 2.4), and a triaxial ellipsoid (Eq. 2.2) to calculate the forces acting on a particle in contact with the air-water interface as a function of the deflection depth  $z_c$ . The force plotted versus deflection depth gives the theoretical force-position curve [Zhang *et al.*, 1996]. We computed these theoretical curves for all particles (PTFE standard particles and natural sediment particles). To compute the forces for the natural particles, we approximated the particle shapes as spheres, cylinders, and ellipsoids, and used the measured shape parameters to calculate maximum and volume-equivalent radii and semi-major axes.

The theoretical calculations provide the maximum force; however, except for the cylindrical particle the snap-off force cannot be calculated because spheres and ellipsoids have no edges on which pinning can occur. A cylindrical particle should ideally have a snap-off force identical to the maximum force in the theoretical force-position curves.

## 2.6 Results and Discussion

### 2.6.1 Interpretation of Force-Position Curves

Figure 2.3 shows an example of a force-position curve for a PTFE sphere. The solid line shows the measured capillary force experienced by the particle as the particle moved through the air-water interface. A zero force indicates that the particle does not experience any net force due to the air-water interface. (The tensiometer balance is tared with the weight of the particle.) A positive force indicates that the particle is being pulled downward, i.e., into the water phase, whereas a negative force indicates that the particle is pulled upward, i.e., out of the water phase (compare Figure 2.1). The single-headed arrows along the



plot show the direction of movement of the particle with respect to the air-water interface (immersion or emersion).

Initially, the particle is in the air-phase (net force is zero), when the particle contacts the air-water interface a downward capillary force (attractive capillary force) is recorded, indicated by the sudden occurrence of a net downward force. The magnitude of the net downward force at this position cannot be interpreted quantitatively because of the particle is attached to the hook at the bottom; however, the snap-in can be detected unequivocally. This position of the air-water interface snap-in at the bottom of the particle is recorded for each particle and the  $z$ -value at this position is set to zero, i.e., our reference position. During the immersion of the particle into the water phase, the force changes from positive to negative and reaches a minimum (or maximum negative force) at a distance of about 6.9 mm. This minimum corresponds to the maximum upward force experienced by the particle (including buoyancy). The air-water interface snaps off the particle just before the force recording becomes constant at a distance of about 8.2 mm. The constant force recorded after snap-off corresponds to the buoyancy. The maximum upward force (repulsive capillary force,  $f_{\max}$ ) and the snap-off force ( $f_{\text{snap-off}}$ ) are then determined by the difference between the recorded minimum force and the buoyancy force.

The emersion curve parallels the immersion curve, but is shifted because of hysteresis of the contact angle. The hysteresis of the contact angle not only affects the maximum forces exerted by the air-water interface, but also changes the position where the maximum forces and snap-off and snap-in occur.

The dashed curve in Figure 2.3 is the rate of change of the capillary force with respect to the change in position in the  $z$ -direction ( $df/dz$ ) of the air-water interface. We use this curve to identify the exact position of the particle with respect the interface where the maximum upward force ( $df/dz = 0$ ) and the snap-off occur ( $df/dz = \max$ ). In the following we present the force-position curves in dimensionless form, so that different particles can be better compared with each other.

## 2.6.2 Theoretical Maximum Capillary Forces and Pressures

Figure 2.4 shows theoretical force-position curves for the immersion of a sphere, an ellipsoid, and a circular cylinder compared with the measured curve for the quartz particle. For the theoretical curves, we assumed that the standard-shaped particles have the same volume as the quartz particle. The spherical particle shows the smallest forces during immersion, because it has the smallest circumference, and the cylinder shows the largest force, because the air-water interface is being pinned at the edges. The ellipsoid gives the closest approximation to the quartz particle in terms of the maximum capillary force.

Capillary forces can be translated to pressure by division by the particle cross-section. Capillary pressures associated with maximum forces were in the range of 100 Pa (Table 2.4, supporting information). This indicates that, in porous

media, the capillary forces on such millimeter-scale particles are important under fairly saturated conditions, for example during infiltration or imbibition.

### 2.6.3 Experimental Maximum and Snap-off Capillary Forces

Figure 2.5 shows the dimensionless force-position curves for the dry PTFE particles of standard shapes and for the quartz particle. We use quartz as example to illustrate the behavior of a natural sediment particle (results for the other sediment particles are shown in Figure 2.12, supporting information). The shape of the curves for the standard particles are related to their geometries. The curves for the PTFE sphere and disk are symmetrical with the immersion and emersion curves almost exact mirror images. Both particles show a large snap-off force, with the disc showing the most pronounced snap-off effect due to interface pinning. The tent and the quartz particle also show snap-off force, due to interface pinning. However, during emersion, there was no snap-in for both the tent and the quartz particle, as the interacting surface area of the particle with the air-water interface is small.

The experimental force-position curves show that particles with a smooth surface show a more pronounced difference between maximum and snap-off forces. The PTFE sphere, with its smooth surface and minimal pinning of the air-water interface, shows a pronounced difference between maximum and snap-off force. The tent shows an even more pronounced difference between the two forces, because the snap-off force is small due the minimal interaction area of the tent tip with the air-water interface. A summary of all the experimental forces is given in Table 2.5 (supporting information).

For the natural particles, the snap-off forces are, in general, smaller than the maximum capillary forces, but in some cases the snap-off force equals the maximum force. This occurs when the air-water interface is pinned at the particle surface strong enough so that snap-off happens under conditions represented by the Gibbs extension of the Young Equation (Eq. 4.3). The more pronounced the pinning, the more likely the air-water interface snaps off at the maximum capillary force.

### 2.6.4 Effect of Solvent Cleaning

We expected that the solvent-cleaning would remove some organic coatings, and therefore, the cleaned particles would have a smaller contact angle than the non-cleaned particles. This should manifest itself in smaller maximum upward and snap-off forces for the solvent-cleaned particles, but this was not observed in all cases. Basalt, milky quartz, hematite, and quartz showed larger forces for cleaned than for uncleaned particles (Tables 2.5, supporting information). Closer examination of the force-distance curves shows that the snap-off forces for these four particles occurred at a greater  $z$  position for the clean particles

compared to the uncleaned particles (Figure 2.5), suggesting that pinning was more pronounced for the clean particles. We infer that surface coatings may have covered and smoothed surface roughness, and that after solvent cleaning, more surface roughness was accessible to the air-water interface.

Figure 2.6 illustrates a complete measurement of force against position for the immersion of a quartz particle in the order they were performed: first the immersion of the dry, uncleaned particle, then the wet, uncleaned particle, followed by the immersion of a cleaned and air-dried particle and lastly for the wet, cleaned particle. The initial, uncleaned dry particle showed large maximum and snap-off forces (solid line). After wetting, the forces decreased, and snap off occurred earlier, indicated by the shift of the  $Z$  position to a smaller value. Similarly, the solvent-cleaned particle showed a left shift of the force-distance curve compared with the uncleaned particle. The solvent-cleaning also made the force-distance curve more symmetrical, indicating the cleaning reduced contact angle hysteresis.

## 2.6.5 Effect of Hysteresis

The immersion and emersion loops of the force-distance curves should, in the ideal case (i.e., in the absence of contact angle hysteresis and surface roughness), be symmetrical. The PTFE sphere indeed had a symmetrical curve, but the natural particles deviated from this symmetry, in some cases considerably (Figures 2.5 and 2.12, supporting information). In general, the emersion curves were smoother than the immersion curves, which we attribute to the smaller contact angle during emersion (receding contact angle).

## 2.6.6 Comparison of Experimental and Theoretical Capillary Forces

Table 3.2 summarizes the experimental and calculated maximum capillary forces. The calculated forces are based on either the volume-equivalent or the maximum radius. The volume-equivalent radius tended to overestimate the measured radius, as shown for the PTFE sphere. For the sphere, the volume-equivalent radius was 14% higher than the measured radius. This led to a larger theoretical capillary force for the volume-equivalent radius than for the maximum radius. The theoretical calculations for the PTFE disc also overestimated the measured value. For the PTFE tent, using the volume-equivalent parameters provided close theoretical force values for both the sphere and the ellipsoidal shape. The theoretical calculations for a circular cylinder shape overestimated the force considerably, because the cylinder shape does take into consideration the linearly reducing cross-section of the tent.

For the natural sediment particles, assuming a spherical shape (sphere) generally lead to an underestimation of the measured capillary force (Table 3.2).

Assuming a circular cylinder, we overestimated the capillary force, whereas the ellipsoidal shape provided the best approximation of the capillary force.

## 2.7 Implications

Previous investigations have shown that capillary forces exerted at the air-water interface can exceed DLVO and gravity forces [Shang *et al.*, 2008; Shang *et al.*, 2009; Preuss and Butt, 1998b; Scheludko *et al.*, 1976], and that moving air-water interfaces during infiltration can mobilize, i.e., detach, soil particles from stationary surfaces [Sharma *et al.*, 2008a; Aramrak *et al.*, 2011; Sharma *et al.*, 2008b]. In porous media, while under dry conditions, the capillary force is a strong attachment force of particles to stationary surfaces, under wet conditions, the capillary force becomes a mechanism of detachment of particles from stationary surfaces. Such wet conditions occur during infiltration or drainage. Here we quantified such detaching capillary forces for differently shaped particles and found that measured capillary forces on natural particles can be approximated by a volume-equivalent ellipsoid. Thus, assuming an ellipsoidal shape allows us to better predict capillary forces experienced by natural particles in porous media. Capillary forces become more important the smaller the particles are, because the gravity force decreases faster with particle size than the capillary force, and the capillary pressure scales inversely with the particle radius. Thus, particularly for particles in the colloidal size range, the capillary forces will play a dominant role.

## 2.8 Tables and Figures

Table 2.1: Maximum capillary forces (experimental and theoretical).

Particle	radius (mm)		capillary force ( $\mu\text{N}$ )					
			experimental (dry, unclean)			theoretical		
	$r_{ve}^\dagger$	$r_{max}^\ddagger$	sphere		$r_{ve}$	cylinder		ellipsoid <sup>*</sup>
			$r_{ve}$	$r_{max}$		$r_{ve}$	$r_{max}$	$r_{max}^{\S\S}$
PTFE sphere	3.17	2.79	-2150	-1652	—	—	—	—
PTFE disc	2.09	2.40	—	—	—	-1510	-1961	—
PTFE tent	2.25	2.99	-1096	-1903	—	-1718	-3000	-1565
basalt	1.15	1.78	-221	-473	-1895	-1161	-738	-423
granite	1.17	1.46	-297	-414	-998	-868	-479	-388
hematite	1.00	1.22	-284	-374	-515	-676	-420	-396
magnetite	0.79	1.16	-180	-298	-389	-637	-377	-432
mica	0.85	1.35	-116	-246	-426	-769	-559	-506
milky quartz	1.07	1.01	-396	-373	-560	-524	-479	-312
quartz	1.13	1.53	-247	-403	-601	-936	-472	-543

<sup>†</sup> volume-equivalent spherical radius

<sup>\*</sup> undulating contact line

<sup>‡</sup> maximum of the three semi-major axes

<sup>§</sup> uses the maximum values of the three semi-major axes of the particle to scale the volume equivalent spherical radius to give a volume-equivalent ellipsoid equal in volume to the real particle

<sup>§§</sup> using the maximum values of the three semi-major axes of the particle, does not give a volume-equivalent particle



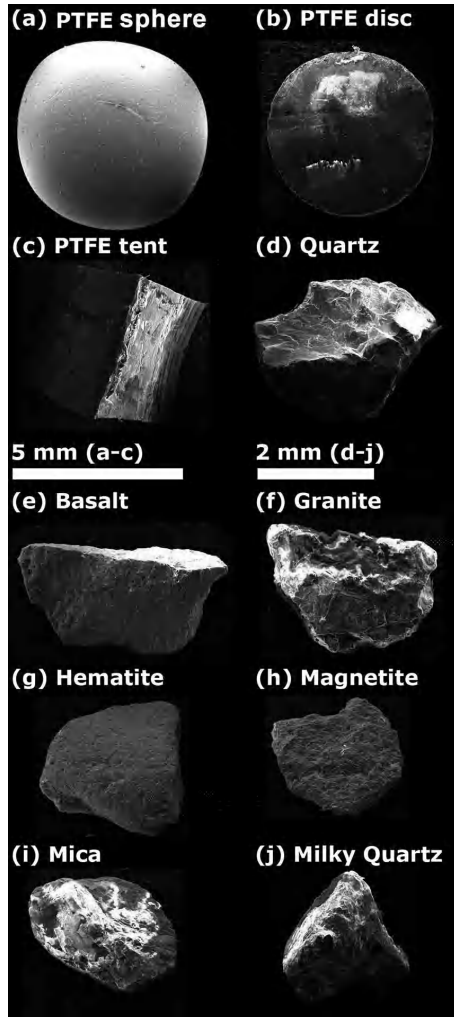


Figure 2.2: PTFE sphere, disc and tent (a–c), and natural sediment particles (d–j) under field emission SEM, viewed perpendicular to the  $xy$ -plane.

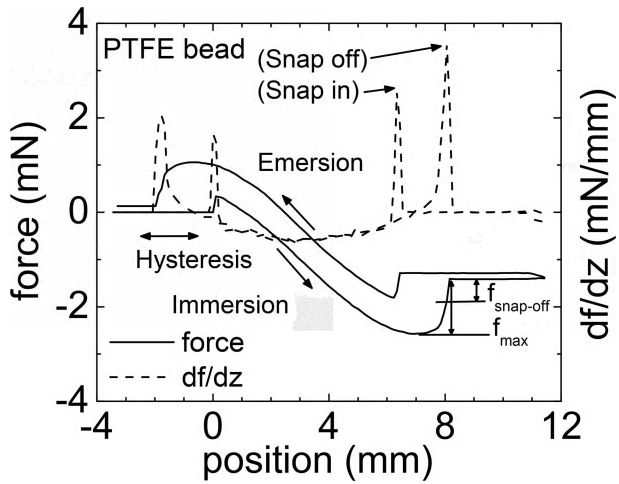


Figure 2.3: Example of a force-position curve for a PTFE sphere ( $r = 2.78$  mm) showing the various segments of the curve during one immersion-emersion cycle and the differentiated force-position curve (dashed line).



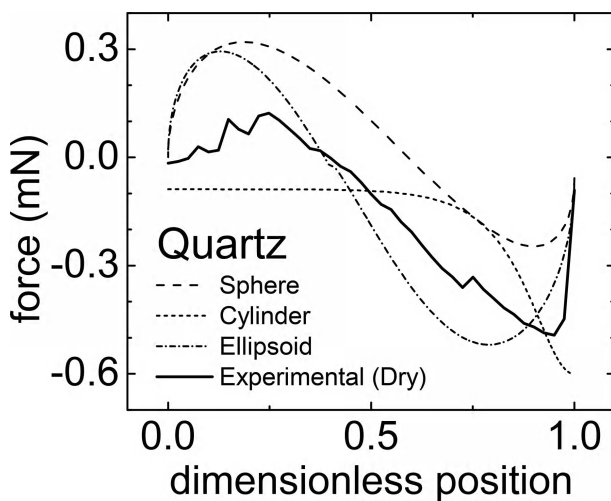


Figure 2.4: Force-position curves of sphere, circular cylinder, and ellipsoid (theoretical) and a dry, uncleaned quartz particle (experimental) during immersion. For the standard shapes, we used the calculated volume-equivalent dimensions ( $r_{ve}$ ) of the quartz particle. [Dimensions of particles in mm are: sphere  $r = 1.13$ ; ellipsoid  $(a, b, c) = (1.47, 1.17, 0.83)$ ; cylinder  $(r, h) = (1.47, 0.83)$ ; quartz  $(x, y, z) = (1.54, 1.22, 0.81)$ ].

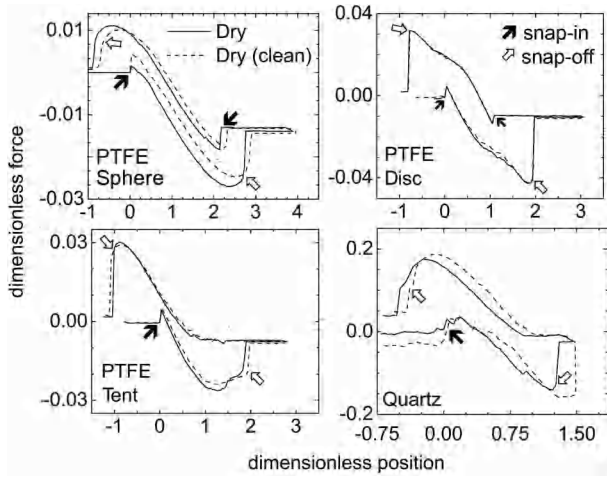


Figure 2.5: Experimental force-position curves of dry PTFE sphere, disc, and tent, and quartz (both cleaned and uncleaned). Filled arrows indicate snap-in, empty arrows indicate snap-off. Dimensions of particles are listed in Table 2.2.

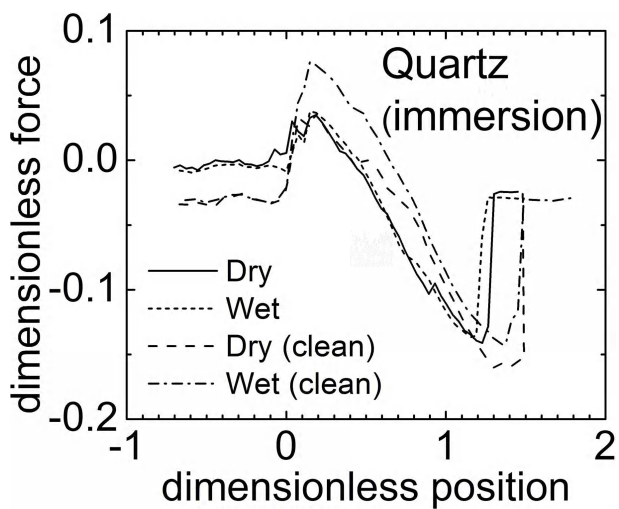


Figure 2.6: Force-position curves of a quartz particle during a sequence of immersion showing changes during the dry and wet stages (both cleaned and uncleaned).

## 2.9 Appendix 2A: Supporting Information

This appendix contains details on the theoretical calculations, measurement precision, calculation of volume-equivalent dimensions. Also given are tables with particle characterization data, experimental force measurements, and particle volume measurements. Figures show dissection scope images of particles, experimental schematics, and force-position plots.

---

**Table of symbols used**

$a, b,$	semi-principal axes of an ellipsoidal particle in the $x, y, z$ coordinate axes	
$c$		
$c_a$	capillary constant	
$e_{xy}$	eccentricity of the ellipses of cross-section on the $xy$ plane containing the contact line	
$e_{xz}$	eccentricity of the ellipse of cross-section on the $xz$ plane normal to both the plane of the contact line and the $y$ -axis	
$f$	total force	$f_b$ buoyancy force
$f_{DLVO}$	DLVO force	$f_p$ hydrostatic pressure force
$f_s$	surface tension force	$f_w$ gravity force
$g$	acceleration due to gravity	$r$ radius of the spherical particle
$x_c$	distance of the three-phase contact line on the $x$ -axis from the vertical ( $z$ -axis)	
$z_c$	deflection depth, i.e., the depth of the well formed in the air-water interface due to the presence of the particle	
$\beta$	the angle of inclination of the projection of the air-water interface at the three-phase contact line on (for an ellipsoidal particle on the surrounding sphere with radius = largest of the semi-major axes, also called the parametric latitude)	
$\Delta p_c$	pressure difference across the air-water interface	
$\phi_c$	the angle of inclination of the air-water interface at the three-phase contact line of a sphere	
$\kappa$	ratio of length of contact line for an ellipsoidal particle (undulating / flat)	
$\gamma$	surface tension of water	$\theta$ contact angle
$\rho_l$	density of liquid phase (water)	$\rho_g$ density of gas phase (air)
$\Delta\rho$	$(\rho_l - \rho_g)$	$\rho_s$ density of solid phase (particle)

---



---

This section was published as supporting information to the journal article: Chatterjee, N., S. Lapin, and M. Flury, (2012), Capillary forces between sediment particles and an air-water interface, *Environ. Sci. Technol.*, **46**, 4411–4418.

### 2.9.1 Derivation of Force Balance on an Ellipsoidal Particle at the Air-Water Interface

We derive the force balance equation for an ellipsoid by generalizing the theory for a sphere. The theory for a sphere has been described previously [Shang *et al.*, 2009; Zhang *et al.*, 1996; Singh and Joseph, 2005]. Here, we use a similar notation as in Zhang *et al.* [1996].

**Sphere:** For a sphere, the gravity and buoyancy forces are given as:

$$f_w = \frac{4}{3}\pi r^3 \rho_s g \quad (2.8)$$

$$f_b = -\frac{\pi}{3}r^3 \rho_l g [2 + 3 \cos(\phi_c + \theta)] - \cos^3(\phi_c + \theta) \quad (2.9)$$

The surface tension force is given as [Zhang *et al.*, 1996; Singh and Joseph, 2005]:

$$\begin{aligned} f_s &= 2\pi x_c \gamma \sin \phi_c \\ &= 2\pi r \gamma \sin(\phi_c + \theta) \sin \phi_c \end{aligned} \quad (2.10)$$

The hydrostatic pressure force is [Zhang *et al.*, 1996; Singh and Joseph, 2005]:

$$\begin{aligned} f_p &= \pi x_c^2 \Delta p_c \\ &= \pi r^2 \rho_l g z_c \sin^2(\phi_c + \theta) \end{aligned} \quad (2.11)$$

Quantitative measurements of the forces exerted by the air-water interface often involve the use of a process tensiometer where the particle is suspended from a microbalance and then dipped into a liquid (Figure 2.10). In such an experimental setup, the microbalance with the particle suspended is tared in the air-phase, so that  $f_{DLVO} = 0$  and  $f_w = 0$ , and the force balance for a sphere (Eq. 3.2) becomes [Shang *et al.*, 2009; Zhang *et al.*, 1996; Singh and Joseph, 2005]:

$$\begin{aligned} f &= 2\pi r \gamma \sin(\phi_c + \theta) \sin \phi_c \\ &\quad + \pi r^2 \Delta \rho g z_c \sin^2(\phi_c + \theta) \\ &\quad - \frac{\pi}{3}r^3 \Delta \rho g [2 + 3 \cos(\phi_c + \theta) - \cos^3(\phi_c + \theta)] \end{aligned} \quad (2.12)$$

**Ellipsoid:** For an ellipsoid (Figure 2.7), the gravity force is given as:

$$f_w = \frac{4}{3}\pi abc \rho_s g \quad (2.13)$$

The buoyancy force for a partially immersed ellipsoid is:

$$f_b = -\frac{\pi}{3}abc \rho_l g \left[ 2 - 3 \cos\left(\beta + \frac{\pi}{2}\right) + \cos^3\left(\beta + \frac{\pi}{2}\right) \right] \quad (2.14)$$

The angle  $\beta$ , also called the parametric latitude, is calculated from the angles  $\theta$  and  $\phi_c$  as:

$$\begin{aligned}\beta &= \arctan \left[ (\sqrt{1 - e_{xz}^2}) \tan \left( \frac{3\pi}{2} - \theta - \phi_c \right) \right] \\ &= \arctan \left[ \frac{c}{a} \tan \left( \frac{3\pi}{2} - \theta - \phi_c \right) \right]\end{aligned}\quad (2.15)$$

where the eccentricities of the elliptic cross-sections,  $e_{xy}$  and  $e_{xz}$  are defined as:

$$e_{xy} = \sqrt{1 - \frac{b^2}{a^2}} \quad (2.16)$$

$$e_{xz} = \sqrt{1 - \frac{c^2}{a^2}} \quad (2.17)$$

The surface tension force, which depends on the length of the three-phase contact line, is given as:

$$f_s = 4a\kappa E(e_{xy})\gamma \sin \phi_c \sin \beta \quad (2.18)$$

where  $E(e_{xy})$  is the complete elliptic integral of the second kind for an ellipse on the  $xy$  plane (plane of the three-phase contact line) and  $\kappa$  is the ratio of the lengths of the undulating contact line to the flat elliptic contact line (see next sub-section). The surface tension force can be either upward (if  $\phi_c + \theta > 180^\circ$ ) or downward (if  $\phi_c + \theta < 180^\circ$ ).

The hydrostatic pressure force is:

$$f_p = \pi ab \Delta p_c = \pi ab \rho_l g z_c \sin^2(\beta) \quad (2.19)$$

For a tared ellipsoidal particle in the air-phase, the final force balance equation (Eq. 3.2) then becomes:

$$\begin{aligned}f &= 4a\kappa E(e_{xy})\gamma \cos \beta \sin \phi_c \\ &+ \pi ab \Delta \rho g z_c \cos^2 \beta \\ &- \frac{\pi}{3} \Delta \rho g abc (2 + 3 \sin \beta - \sin^3 \beta)\end{aligned}\quad (2.20)$$

## 2.9.2 Calculating the Undulating Quadrupolar Contact Line on an Ellipsoidal Particle

Previous work has shown that the contact line at the liquid-gas interface on an asymmetric particle, like an ellipsoid, is not planar, but in fact undulates, and can be described using a quadrupolar expansion [Brown *et al.*, 2000; Stamou *et al.*, 2000; Fournier and Galatola, 2002; Danov *et al.*, 2005; van Nierop *et al.*,

2005; *Lehle et al.*, 2008; *Danov and Kralchevsky*, 2010]. We used the approach of *van Nierop et al.* [2005]. to calculate the undulation of the interface line for an ellipsoid. We assume that the mean position of the contact line is the same as the one at a flat contact line, as would be present on a symmetrical (i.e., circular cross-section) particle.

The undulation is described as a deviation of the contact line from its mean position on the  $z$ -axis. The deviation  $z_{dev}$  on the the  $z$ -axis is calculated as a solution of the equation [*van Nierop et al.*, 2005]:

$$\sum_{n=1}^{\infty} \frac{C_n \cos(2n\varphi)(1 - e_{xy}^2 \cos^2 \varphi)^n}{\{1 - (z_{dev} - C_0)^2\}^n} - z_{dev} = 0 \quad (2.21)$$

where  $-\pi \leq \varphi \leq \pi$  is the azimuthal angle of the point where  $z_{dev}$  is to be calculated,  $C_0$  and  $C_n$  are coefficients, and  $e_{xy}$  is the eccentricity of the elliptic cross-section at the contact line (see Eq. 2.16).

The series was summed until  $n = 2$  as the contribution of higher-order terms quickly falls off. The resulting undulations  $z_{dev}$  were two orders of magnitude smaller ( $< 1\%$ ) than the respective  $c$  values (semi-major axis on the  $z$ -axis) of the particle. An optimization of the coefficients  $C_n$ , which enforces the contact angle between the air-water interface and the ellipsoidal surface was thus not attempted. The initial set of  $C_n$  used was  $[C_0, C_1, C_2] = -\cos(\theta)[1, 0.01, 0.0001]$ . [*van Nierop et al.*, 2005]

The length of the undulating contact line was calculated by summing the distance between the previously calculated points using Eq. 2.21. A similar calculation was done assuming a flat, elliptic contact line. The increase in contact line due to the undulation was expressed as  $\kappa$ , the length ratio of the undulating line to the flat line (Table 2.4). The effect of the undulating contact line length is an increase of the capillary force (Table 2.4).

### 2.9.3 Calculation of a Volume-Equivalent Radius and Semi-Major Axes for a Particle

For each particle we calculated a volume-equivalent radius, corresponding to the radius of a sphere with the same volume as the particle, as well as the semi-major axes corresponding to a volume-equivalent ellipsoid. To determine the particle volume, we measured the buoyancy force from the force-position curves of the dry particle at the point just after the snap-off of the air-water interface. The measured buoyancy force was then corrected for the buoyancy of the submerged portion of the steel J-hook attached to the particle (Figure 2.10) as well as for the surface tension force on the submerged part of the hook. The corrected buoyancy force,  $f_{buoy,corr}$  is given as:

$$f_{b, corr} = f_{b, uncorr} - f_{b, hook} + f_{s, hook} \quad (2.22)$$

The volume of a particle,  $v_p$ , and the volume-equivalent spherical radius,  $r_{ve}$ , are calculated as:

$$v_p = \frac{f_{b, \text{corr}}}{\rho_l g} \quad (2.23)$$

$$r_{ve} = \sqrt[3]{\frac{3v_p}{4\pi}} \quad (2.24)$$

The volume-equivalent ellipsoidal semi-major axes  $(a, b, c)_{ve}$  were calculated using the spherical  $r_{ve}$  scaled with the rms values of the semi-major axes  $(a, b, c)_{rms}$ , this keeps the volume of the ellipsoid equal to that of the natural particle (and the volume-equivalent sphere). Also, the maximum semi-major axes  $(a, b, c)_{max}$  were used to construct an encompassing ellipsoid of maximum dimensions ( $r_{max}$ ) for comparison to the volume-equivalent ellipsoid. A schematic of the process is shown in Figure 2.8. The particle volume and the rms dimension along the  $z$  axis ( $c_{rms}$ ) were used to calculate the radius for the cylinder, which were used in theoretical calculations involving a volume-equivalent cylinder. Results are summarized in Tables 2.2 and 2.3.

## 2.9.4 Errors of Force-Position Measurements

### Errors due to change in surface tension of water

For each particle's sequence of measurements, we used the same water in the glass cup, but we changed the water for every new particle. We measured the surface tension of the water before and after the determination of each force-position curve with the Wilhelmy plate method. The surface tension of water before immersion of the particle was  $72.4 \pm 0.4$  mN/m, while the surface tension after the uncleaned particle had been immersed was  $65.8 \pm 3.2$  mN/m for basalt, hematite, and mica, and  $72.1 \pm 0.3$  mN/m for the other particles. As the surface tension of the water changed by  $\approx 10\%$  between the start and end of a force-distance sequence, our force measurements are erroneous to maximal 10% when comparing cleaned and uncleaned particle data.

### Errors due to randomness in roughness of particle surfaces

Figure 2.11 depicts the precision (measurement error) in the measurement of the capillary forces, illustrated for a smooth particle (PTFE sphere) and a natural sediment particle (quartz). Generally, the errors were larger for the sediment particle than the standard particles because of the slipping and pinning of the interface line caused by surface roughness. The plots show that the standard deviations were largest when the changes of forces with respect to position ( $\Delta f / \Delta z$ ) were greatest, i.e., when snap-off of the interface occurred. This is because the position where snap-off occurs depends on surface roughness, and depending on the degree of surface roughness, snap-off may not occur always at exactly the



same location. This effect is more pronounced for the irregularly-shaped quartz particle (Figure 2.11b) than for the PTFE sphere (Figure 2.11a).

Table 2.2: Particle characterization in terms of spatial dimensions and contact angle with an air-water interface.

Particle	$r_{ve}^{\S}$ (mm)	$x_{max}^*$ (mm)	$x_{rms}^{\S\S}$ (mm)	$y_{max}^*$ (mm)	$y_{rms}^{\S\S}$ (mm)	$z_{max}^*$ (mm)	$z_{rms}^{\S\S}$ (mm)	contact angle <sup>†</sup> (°)
PTFE sphere <sup>†</sup>	3.17	5.59	—	5.56	—	5.57	—	109±5
PTFE disc <sup>†</sup>	2.09	4.81 <sup>d</sup>	—	—	—	2.22 <sup>t</sup>	—	109±5
PTFE tent <sup>†</sup>	2.25	5.99 <sup>l</sup>	—	4.75 <sup>b</sup>	—	3.45 <sup>h</sup>	—	109±5
Basalt	1.15	3.56	2.64	1.88	1.51	0.96	0.79	67±3
Granite	1.17	2.92	2.29	2.15	1.62	1.73	1.30	83±2
Hematite	1.00	2.45	1.99	2.27	1.90	1.47	1.07	95±1
Magnetite	0.79	2.32	1.72	2.01	1.42	0.95	0.75	84±2
Mica	0.85	2.71	2.16	1.79	1.44	0.97	0.69	58±3
Milky Quartz	1.07	2.03	1.58	1.92	1.50	1.69	1.21	117±2
Quartz	1.13	3.07	2.27	2.44	1.81	1.61	1.28	75±2

<sup>†</sup> single measurements for all PTFE particles hence no rms values are reported

<sup>§</sup> volume-equivalent radius

<sup>§§</sup> root mean square dimension

<sup>d,t</sup> diameter & thickness of PTFE disc

<sup>\*</sup> maximum dimension

<sup>†</sup> contact angle for cleaned particles

<sup>l,b,h</sup> base length, base breadth & height of PTFE tent

Table 2.3: Particle volume, radius of volume-equivalent sphere ( $r_{ve}$ ) and semi-major axes of volume-equivalent ellipsoids (using both maximum  $a : b : c$  and root-mean-square (rms)  $a : b : c$  ratios).

Particle	volume (mm <sup>3</sup> )	$r_{ve}$ (mm)	rms (mm)			maximum (mm)		
			$a$	$b$	$c$	$a$	$b$	$c$
PTFE sphere	133.90	3.17	3.18	3.17	3.17	3.18	3.17	3.17
PTFE disk	38.17	2.09	2.70	2.70	1.25	2.70	2.70	1.25
PTFE tent	47.51	2.25	2.92	2.31	1.68	2.92	2.31	1.68
Basalt	6.40	1.15	2.07	1.18	0.62	2.21	1.16	0.59
Granite	6.73	1.17	1.58	1.12	0.90	1.54	1.14	0.91
Hematite	4.13	1.00	1.19	1.25	0.67	1.21	1.12	0.73
Magnetite	2.03	0.79	1.11	0.91	0.48	1.11	0.96	0.45
Mica	2.58	0.85	1.42	0.95	0.46	1.38	0.91	0.49
Milky Quartz	5.06	1.07	1.18	1.12	0.91	1.15	1.09	0.96
Quartz	5.97	1.13	1.47	1.17	0.83	1.51	1.20	0.79

Table 2.4: Experimental and theoretical maximum forces, percentage increase in contact line due to undulations, and capillary pressures.

Particle	contact angle (°)	maximum force ( $\mu\text{N}$ )				area <sup>§§</sup> mm <sup>2</sup>	ratio <sup>*</sup> $\kappa$	pressure Pa
		experimental	theoretical <sup>§</sup>					
			flat	undulating				
PTFE sphere	109±5	-1305	-2150 <sup>†</sup>	—	16.31	—	-132	
PTFE disc	109±5	-1292	-1961 <sup>†</sup>	—	16.47	—	-119	
PTFE tent	109±5	-1204	-1327	-1446	14.27	1.090	-93	
Basalt	67±3	-537	-697	-738	9.12	1.060	-76	
Granite	83±2	-467	-440	-479	4.08	1.090	-108	
Hematite	95±1	-279	-396	-420	2.79	1.060	-142	
Magnetite	84±2	-422	-346	-377	2.53	1.089	-137	
Mica	58±3	-526	-514	-559	3.99	1.087	-129	
Milky Quartz	117±2	-7	-451	-479	2.92	1.061	-155	
Quartz	75±2	-402	-433	-472	4.00	1.090	-108	

Theoretical calculations assuming: <sup>§</sup>ellipsoidal, <sup>†</sup>spherical or <sup>‡</sup>cylindrical shapes

<sup>§§</sup> cross-sectional area at same  $z$ -axis position where maximum force occurs

<sup>\*</sup> ratio of the length of a quadrupolarly undulating, elliptic contact line to a flat elliptic contact line

Table 2.5: Experimental maximum and snap-off capillary forces for different particles.

Particle	contact angle ( $^{\circ}$ )	$r_{max}$ (mm)	$f_{max}$ , maximum force ( $\mu\text{N}$ )			$f_{snap-off}$ , snap-off force ( $\mu\text{N}$ )		
			Dry	Dry Clean	Wet	Dry	Dry Clean	Wet
PTFE sphere	$109 \pm 5$	2.79	-1305	-1022	-1163	-879	-534	-466
PTFE disc	$109 \pm 5$	2.41	-1292	-1281	-1260	-1169	-778	-1207
PTFE tent	$109 \pm 5$	2.99	-1204	-1081	-1023	-397	-412	-746
Basalt	$67 \pm 3$	1.78	-537	-597	-525	-537	-533	-312
Granite	$83 \pm 2$	1.46	-467	-502	-444	-427	-497	-352
Hematite	$95 \pm 1$	1.23	-279	-322	-38	-249	-161	-26
Magnetite	$84 \pm 2$	1.16	-422	-149	-329	-378	-94	-273
Mica	$58 \pm 3$	1.36	-526	-43	-470	-348	-39	-309
Milky Quartz	$117 \pm 2$	1.01	-7	-541	-10	-7	-426	-6
Quartz	$75 \pm 2$	1.54	-402	-474	-377	-357	-445	-268

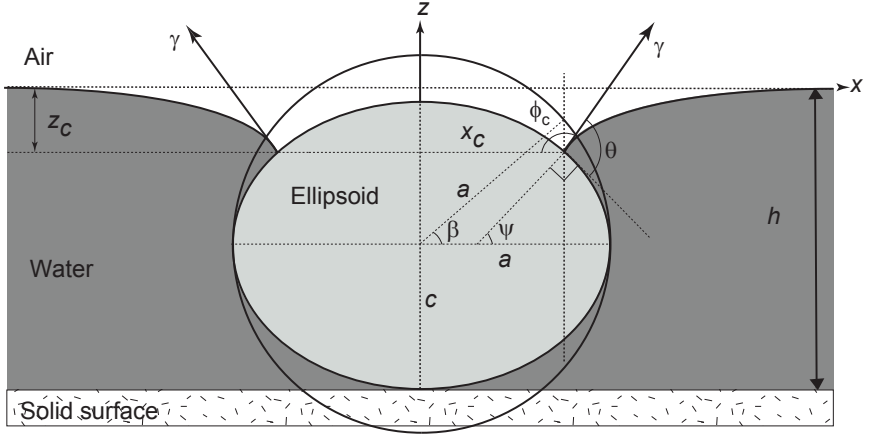


Figure 2.7: Schematic of an ellipsoidal particle at an air-water interface.  $\theta$  is the contact angle, the angle between the tangents to the ellipsoidal particle and the air-water interface at the contact line.  $\psi$  is the geodetic latitude, the angle of the normal to the tangent at the three-phase contact line with the plane parallel to the undisturbed air-water interface containing the center of the ellipsoid.  $\beta$ ; the parametric latitude, is the angle of the projected contact line at the center of the ellipsoid. The projection is done on the surrounding sphere (of radius  $a$ , where  $a$  is the largest of the ellipsoid's semi-major axes).  $\psi = [\frac{3\pi}{2} - (\theta + \phi_c)]$ .  $\beta = \arctan[\frac{c}{a} \tan \phi]$ .

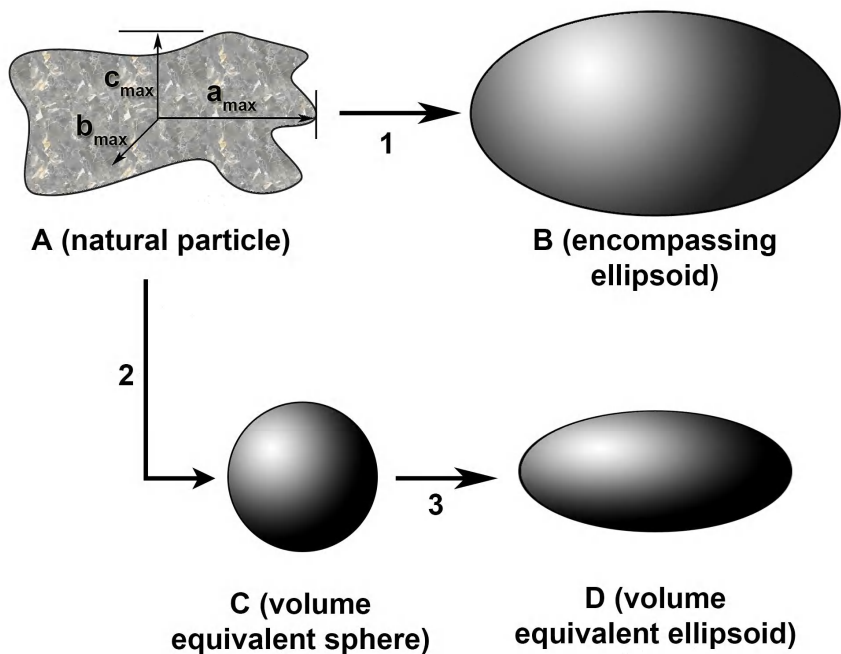


Figure 2.8: Schematic of calculation steps to determine volume-equivalent standard shapes from the dimensions of the natural particles. (1) Define a maximum encompassing ellipsoid (B) from the  $(a, b, c)_{max}$  dimensions of the natural particle (A). The resulting particle (B) is, however, not volume equivalent with the natural particle (A). (2) Determine a volume-equivalent sphere (C) from the buoyancy force on the natural particle (A). (3) Determine a volume equivalent ellipsoid (D) using the volume of (C) and the ratios of the rms semi-major axes,  $(a, b, c)_{rms}$ .

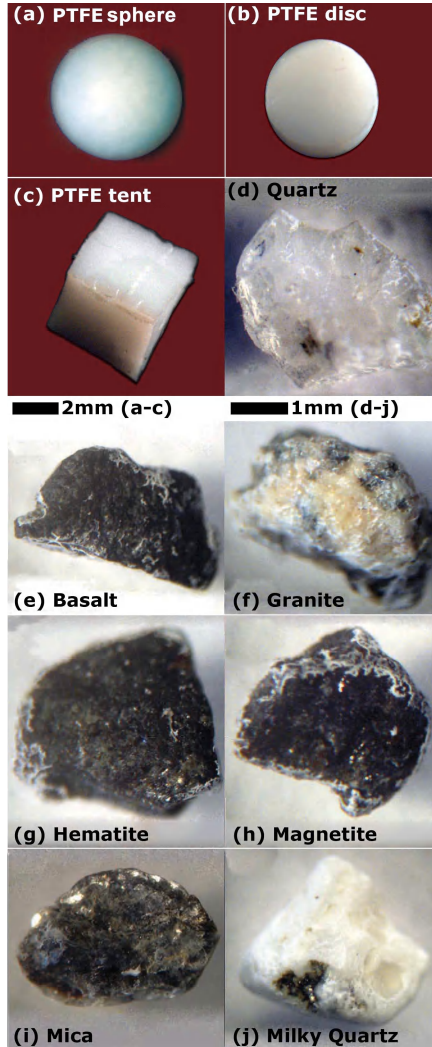


Figure 2.9: PTFE sphere, disc and tent (a–c) and natural sediment particles (d–j) under dissection scope, viewed perpendicular to the  $xy$ -plane.



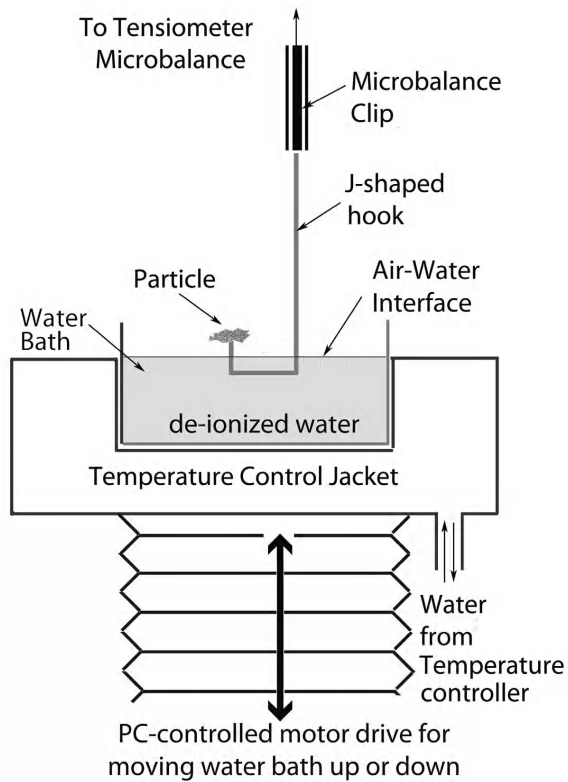


Figure 2.10: Schematic of capillary force measurements with a process tensiometer.

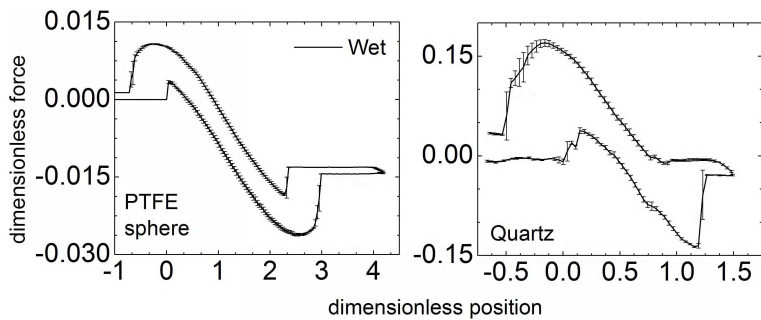


Figure 2.11: Force-position curves illustrating measurement precision for (a) a wet PTFE sphere and (b) a wet quartz particle. Data represent the mean and  $\pm$  one standard deviation of five successive measurements.

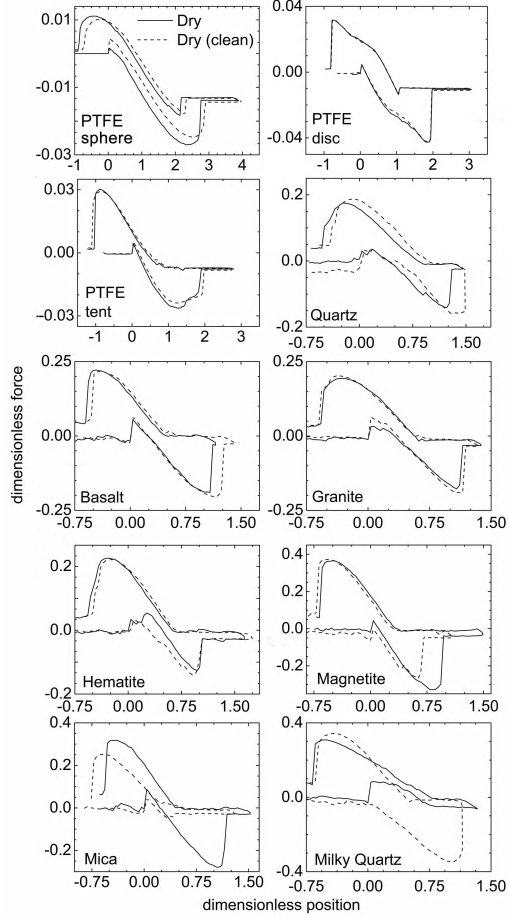


Figure 2.12: Dimensionless force-position curves of dry PTFE particles (sphere, disc, and tent) and natural particles (both cleaned and uncleaned).

## 2.10 Appendix 2B: MatLab Code for Calculating Capillary Rise (Ellipsoidal Particle)

ELL.M

```
phi_c=zeros(50,1);
x_c=zeros(50,1);
z_c=zeros(50,1);
n=zeros(200,1);
R=0.26;                                % dimensionless radius
                                       % phi=[0:1:180]

x=[3.2:0.001:3.3];
phi_0=0.1/180*pi;    % initial angle of the interface set to
                     % a non-zero small value

for i=1:101;                % Iteration counter
    x_0=x(i);              % initial x
    z_0=-besselk(0,x_0)/besselk(1,x_0)*sin(phi_0); % define initial z
    y_0=[x_0,z_0];         % the dimensionless point (x, z)
                           % on the liquid-gas interface.

    tspan=[-pi:0.001:pi];    % angular range from phi_0 to pi
    [t,y] = ode45(@myfun3,tspan,y_0); % solve for optimal value of z
                                       % (the capillary rise)

    for j=1:2000            % Finding the point y(j,1)=R*sin(n(j)) the difference
                           % between y(j,1) and R*sin(n(j)) is less than 0.0001
                           % (tolerance)

        n(j)=82/180*pi+t(j);                % add contact angle
        if abs(y(j,1)-R*sin(n(j)))<0.0001 % tolerance check
            phi_c(i)=t(j);
            x_c(i)=y(j,1);
            z_c(i)=y(j,2);
            break
        end
    end
end

% plot capillary rise for radial positions on the x-axis
plot(y(:,1),y(:,2), 'LineWidth',2);
xlabel('Position (x) (arbitrary units)');
ylabel('Capillary Rise (z) (arbitrary units)');
```

## MYFUN3.M

```
function dy = myfun3(t,y)
dy = zeros(2,1); % a column vector
dy(1) = -cos(t)/(y(2)+sin(t)/y(1));
dy(2) = sin(t)/(y(2)+sin(t)/y(1));
```

## OUTPUT

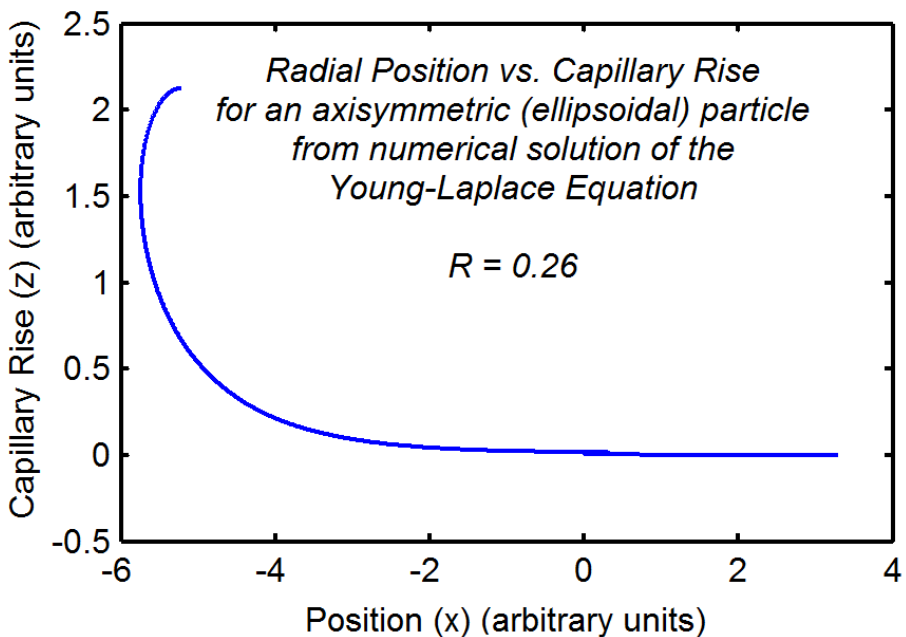


Figure 2.13: Output from MatLab code in `e11.m`. Radial position on particle surface ( $x$ ) vs. Capillary rise ( $z$ ) for a generic ellipsoid. The  $R$  value is a dimensionless radius parameter.



# Chapter 3

## Effect of Particle Shape on Capillary Forces Acting on Particles at the Air-Water Interface

### 3.1 Abstract

The capillary forces exerted by moving air-water interfaces can dislodge particles from stationary surfaces. The magnitude of the capillary forces depends on particle shape, orientation, and surface properties, such as contact angle and roughness. The objective was to quantify, both experimentally and theoretically, capillary force variations as an air-water interface moves over the particles. We measured capillary forces as a function of position, i.e., force-position curves, on particles of different shape by using force tensiometry. The particles (5-mm nominal size) were made of polyacrylate and were fabricated using a 3D printer. Experimental measurements were compared with theoretical calculations. We found that force-position curves could be classified into three categories according to particle shapes: (1) curves for particles with round cross-sections, such as spheroidal particles, (2) curves for particles with fixed cross-sections, such cylindrical or cubical particles, and (3) curves for particles with tapering cross-sections, such as prismatic or tetrahedral particles. Spheroidal particles showed a continuously varying capillary force. Cylindrical or cubical particles showed pronounced pinning of the air-water interface line at edges. The pinning led to an increased capillary force, which was relaxed when the interface snapped off from the edges. Particles with tapering cross-section did not show pinning

and showed reduced capillary forces as the air-water interface line perimeter and displacement cross section continuously decrease when the air-water interface moved over the particles.

## 3.2 Introduction

Air-water interfaces play an important role in many physical phenomena occurring in nature [de Gennes *et al.*, 2004]. A prominent example is the capillary force, which acts when a solid comes into contact with an air-water interface. The capillary force gives rise to capillary rise of water in a porous medium and to attachment of particles at the air-water interface. The strong attachment of particles to the air-water interface provides mechanisms for cleaning of wafers in microelectronics [Leenaars and O'Brien, 1989; Noordmans *et al.*, 1997; Gomez-Suarez *et al.*, 1999b; Gomez-Suarez *et al.*, 1999a], as well as for immobilization [Wan and Tokunaga, 1997; Veerapaneni *et al.*, 2000] and mobilization of particles in porous media [Zhuang *et al.*, 2007; Shang *et al.*, 2008; Sharma *et al.*, 2008a; Cheng and Saiers, 2009].

Particles in contact with an air-water interface experience a force due to the surface tension and the pressure caused by the curvature of the air-water interface. The capillary force is the sum of the surface tension and pressure forces. The capillary force can exceed other interparticle forces, such as DLVO forces [Scheludko *et al.*, 1976; Preuss and Butt, 1998a; Sharma *et al.*, 2008b; Shang *et al.*, 2009], thereby leading to detachment and mobilization of particles from stationary surfaces [Leenaars and O'Brien, 1989; Noordmans *et al.*, 1997; Gomez-Suarez *et al.*, 1999b; Shang *et al.*, 2008; Aramrak *et al.*, 2011; Lazouskaya *et al.*, 2011; Aramrak *et al.*, 2013].

The capillary force acting on macroscopic particles has been quantified experimentally with force tensiometry [Shang *et al.*, 2008; Zhang *et al.*, 1996; Zhang *et al.*, 1997; Chatterjee *et al.*, 2012]. Capillary forces acting on microscopic particles, mostly spheres, have been measured by using atomic force microscopy [Preuss and Butt, 1998a; Preuss and Butt, 1998b; Gillies *et al.*, 2005; Englert *et al.*, 2009; Yamamoto *et al.*, 2010]. While most of these measurements have been conducted on spherical or spheroidal particles [Gunde *et al.*, 1995; Ecke *et al.*, 1999], more recently, measurements with irregularly-shaped particles and natural mineral particles have been reported [Shang *et al.*, 2008; Chatterjee *et al.*, 2012].

These measurements with irregularly-shaped particles have shown that the shape and surface roughness play an important role in the interaction of the air-water interface with the particle. Natural particles often have sharp corners and edges from mechanical weathering and chipping, smooth, rounded faces from tumbling and from air and water erosion, and rough eroded surfaces due to chemical weathering—all on the same particle. Also, the characteristics of the mineral type lends to particular particle shapes, e.g., clay mineral particles tend to have



flat plate-like shapes, while basaltic and granitic minerals have more granular, non-plate-like shapes. The presence of multiple such surface morphologies and features cause irregular particles to experience capillary forces which are a combination of features of multiple types of particle shapes. Particles with edges contribute to pinning of moving air-water interfaces at the edges, while corners oriented along the direction of the interface movement can cause progressive lowering of the capillary force as cross-sections of the particles reduce gradually. The capillary force-position curves for irregular particles thus show a combination of features like abrupt force changes associated with interface pinning and snap-off, and rounded and gradually reducing sections and random force variations from local roughness features.

The capillary force can theoretically be calculated with the Young-Laplace equation. Only in special cases the Young-Laplace equation has an analytical solution. Numerical calculations of capillary forces have been reported for spherical particles [Zhang *et al.*, 1996; Zhang *et al.*, 1997; Ecke *et al.*, 1999; Princen, 1969]. Axisymmetric, but non-spherical, particle shapes have also been used for theoretical calculations [Chatterjee *et al.*, 2012; Hesla and Joseph, 2004; Singh and Joseph, 2005], but calculations become more complicated. No theoretical calculations have been reported for irregularly-shaped particles.

Surface roughness affects the magnitude of the capillary force. The air-water interface can get pinned at macroscopic (e.g., corners, edges) and microscopic (e.g., surface irregularities) roughness. The pinning usually leads to an increase of the capillary force [de Gennes *et al.*, 2004; Chatterjee *et al.*, 2012; Ally *et al.*, 2012] and to a slip-pin behavior of a moving air-water interface. As most natural particles have rough surfaces, the slip-pin behavior of moving air-water interfaces is expected to be a common phenomenon.

In previous studies by our group, we have measured capillary forces using tensiometry on regularly- and irregularly-shaped particles [Shang *et al.*, 2009; Chatterjee *et al.*, 2012]. Here, we expand on our previous studies by systematically investigating the effects of particle shapes on capillary forces. The objective of this study was to analyze, both theoretically and experimentally, the effect of particle shape on the capillary forces between the particles and the air-water interface. We experimentally measured the capillary force as a function of position, i.e., force-position curves, and we reconstructed the theoretical force-position curves based on numerical solutions of the Young-Laplace equation. We then compared the theoretical calculations with experimental measurements and deduced the specific topological features giving rise to the force-distance curve characteristics.

## 3.3 Theory

### 3.3.1 Capillary Force

The theoretical basis of capillary force calculations involves numerically solving the Young-Laplace equation. Let us consider a particle in contact with a horizontal air-water interface, with the coordinate system comprising of the horizontal  $x, y$ -axes and the vertical  $z$ -axis. The theoretical capillary rise,  $z_c$ , against a surface of a solid particle can be calculated assuming that the air-water interface, at an extended distance ( $x \rightarrow \infty$ ) from the axis of the particle, is undistorted and horizontal. For this case, the relationship between the capillary rise  $z_c$ , the horizontal distance of the contact line on the particle surface formed by the air-water interface from the  $z$ -axis,  $x_c$ , and the angle of inclination of the curved interface from the undisturbed interface,  $\phi_c$ , is [Shang *et al.*, 2009; Zhang *et al.*, 1996; Chatterjee *et al.*, 2012]:

$$z_c = \frac{k_0(x_c)}{k_1(x_c)} \sin \phi_c \quad (3.1)$$

where the functions  $k_0(x)$  and  $k_1(x)$  are the modified Bessel functions of the second kind of orders 0 and 1, respectively.

The details of the calculation of capillary forces for axisymmetric particles are described in Zhang *et al.* [1996]. For non-spherical, axisymmetric particles, the capillary force vectors give rise to an undulating, multipolar force field. This multipolar force field has been observed experimentally [Loudet *et al.*, 2005; Loudet *et al.*, 2006; Lewandowski *et al.*, 2008] and characterized theoretically [Stamou *et al.*, 2000; Kralchevsky *et al.*, 2001; Danov *et al.*, 2005; van Nierop *et al.*, 2005; Lehle and Oettel, 2007; Lehle *et al.*, 2008; Danov and Kralchevsky, 2010].

In our previous work, we have measured and calculated capillary forces on natural sediment particles and model particles, and we calculated theoretical forces on the sediment particles assuming them to be triaxial ellipsoids [Chatterjee *et al.*, 2012]. We now extend our previous work to theoretically construct the force-position curves for a variety of particle shapes and compare them with experimental curves. In this work, we numerically solve for the capillary rise for each particle with the boundary conditions dictated by their respective geometries. Following the approach described by Zhang *et al.* [1996], Shang *et al.* [2009], and Chatterjee *et al.* [2012], we calculate the force balance on a particle in contact with the air-water interface as:

$$f = f_s + f_p + f_b = f_{cap} + f_b \quad (3.2)$$

where  $f$  is the net force on the particle, and,  $f_s$ ,  $f_b$ , and  $f_p$  are surface tension, buoyancy, and pressure forces, respectively, and  $f_{cap} = f_s + f_p$  is the capillary force. We assume the particle to be tared in the air phase, so the gravitational force can be omitted in Equation 3.2.

When the particle is non-axisymmetric or when surface inhomogeneities are present, the contact line itself is undulating [Loudet *et al.*, 2005; Loudet *et al.*, 2006; Stamou *et al.*, 2000; Kralchevsky *et al.*, 2001; Lehle *et al.*, 2008]. However, these undulations do not increase the length of the contact line more than 10% [Chatterjee *et al.*, 2012]; thus, for mathematical simplicity, we do not correct for the increased length of the contact line. The three force components,  $f_s$ ,  $f_b$ , and  $f_p$ , are calculated according to the geometry of the particle shape. The surface tension force,  $f_s$ , depends on the length of the contact line interacting with the air-water interface, the pressure force,  $f_p$ , depends on the area of the cross-section at the plane of the contact line, and the buoyancy force,  $f_b$ , depends on the volume of the particle submerged under the air-water interface at the particular position.

### 3.3.2 Gibbs' Inequality

On an ideal particle with a smooth surface, the moving interface adjusts to an equilibrium position, with the contact angle at an equilibrium value for the particular three-phase interface. In a situation where a moving air-water interface interacts with a rough or edged particle, the roughness of the particle surface causes the interface to be attached at edges under non-equilibrium conditions. The non-equilibrium condition is manifested as a pinning of the air-water interface with a contact angle considerably different from the equilibrium contact angle. The range of values of the contact angle can be mathematically formulated by the Gibbs extension of the Young equation [Singh and Joseph, 2005]:

$$\theta_0 < \theta < 180^\circ - \alpha + \theta_0 \quad (3.3)$$

where  $\theta_0$  is the equilibrium contact angle for a smooth surface,  $\theta$  is the non-equilibrium contact angle due to pinning of the air-water interface at the edge, and  $\alpha$  is the wedge angle measured through the particles' solid phase. For example, for a cubical particle, the wedge angle is  $90^\circ$  at the cube's top or bottom edges. The edge causes the interface to get pinned and distorted, compared to a smooth surface without edges. As Equation 3.3 shows, the pinning causes the actual contact angle to exceed the equilibrium contact angle. This increasing contact angle and the distortion of the air-water interface cause the capillary force to increase. When the contact angle passes a critical value, given by the Gibbs inequality, the air-water interface contact line snaps off from the edge and forms again at a new equilibrium position.

## 3.4 Experimental Section

### 3.4.1 Model Particles

The capillary force measurements were done on mm-scale, UV-cured polyacrylate plastic particles made using a 3D printer. The density of the UV-cured polyacrylate plastic material was  $1.09 \text{ g/cm}^3$ . We made nine particles of standard shape, and categorized the particles according to their surface geometry and cross-section of interaction with the air-water interface (Fig. 3.1). First, we made a digital model of the particles by using the open source 3D modeling software Blender (Version 2.6.3) and saved it as a stereolithography (.stl) file. The model particles were attached to a 0.5-mm thick common base plate using cylindrical stands (1-mm o.d.  $\times$  1-cm length) to facilitate single-piece fabrication during printing (Fig. 3.1 inset). The .stl file was sent to Shapeways Inc. ([www.shapeways.com](http://www.shapeways.com)) for 3D printing. Dimensions of the manufactured particles were measured using a digital caliper (Digit-Cal mm2000, Brown & Sharpe, Providence, RI) and are listed in Table 4.1.

Based on the variation of the cross-section interacting with the air-water interface, the particles can be classified into three main types (Fig. 3.2): (a) particles with continuously varying cross-section (sphere and ellipsoid), (b) particles with a fixed cross-section (cylinder, hexagonal cylinder, and cube), and (c) particles with a linearly reducing or tapered cross-section [cone, square pyramid, tetrahedron, and trigonal prism (tent-shaped)]. For further discussion of Fig. 3.2 see Section 3.5.1.

After printing, the individual particles were detached from the base plate and the attaching stands were cut off. The particles were then characterized for surface roughness and air-water contact angles. The magnified views of the particles in Fig. 3.3 show evidence of roughness due to the limited resolution of the 3D printer. The manufacture specified resolution of the printer was  $100 \text{ }\mu\text{m}$  (<http://www.shapeways.com/materials/frosted-detail-design-guidelines>). The air-water-particle surface contact angle on the particles was determined with a goniometer (CA Goniometer Model 50-00-115, Ramé-Hart Instrument Co., Netcong, NJ) using the method described in Chatterjee et al.[Chatterjee et al., 2012]. For the contact angle measurements, the particles were cleaned with ethanol and deionized water, dried, and then mounted on glass microscopy slides using double-sided adhesive tape. A micro-syringe (steel needle with diameter of 0.5 mm) was used to put a  $25 \text{ }\mu\text{L}$  drop of water just next to the edge of the particle, so that the particle touched the side of the drop. The static contact angle of the particle material (UV-cured polyacrylate) was measured to be  $136^\circ \pm 2^\circ$ . The advancing and receding contact angles were measured on an expanding and a contracting drop of water, respectively, placed on the polyacrylate surface of the detached base plate. The advancing contact angle was  $151^\circ \pm 2^\circ$  and the receding contact angle was  $134^\circ \pm 4^\circ$ .

### 3.4.2 Capillary Force Measurements

The particles were mounted on the lower end of J-shaped steel hooks using a small amount of polyacrylate glue (Dr. Bond Superglue, ITW Inc., Solon, OH). Prior to the measurement of the force-position curves, the mounted particles were cleaned with ethanol and deionized water, and then dried in a jet of air. The details of recording the force-position curves on the tensiometer (Processor Tensiometer K100, Krüss GmbH, Hamburg, Germany) was described in detail previously [Chatterjee *et al.*, 2012]. Briefly, to determine the force-position curves, the upper end of the hook of a mounted particle was inserted into the tensiometer microbalance balance clip, and the microbalance was tared with the particle and hook in the air phase (Fig. 4.1). An air-water interface was then moved over the stationary particle by incrementally raising a beaker of water at a speed of 6 mm/min. The forces exerted on the particle as a function of position of the air-water interface was recorded to generate a force-position curve till the air-water interface passed the top of the particle and the particle was fully immersed in water. For each particle, we recorded five replicate runs of the force-position curve, and then averaged the data.

### 3.4.3 Surface Characterization with SEM

After the determination of the force-position curves, the particles were detached from the J-shaped hook, and coated with platinum-palladium to a thickness of 3 nm under a sputter coater (Model 108auto, Cressington Scientific, Watford, England). We then examined the particles under a scanning electron microscope (SEM) equipped with a field emission electron gun (FEI Quanta 200F, FEI Co., Hillsboro, OR). The particles were kept oriented under the SEM in the same manner as for the force-position and contact angle measurements. If observed directly from the top, we obtain the  $xy$ -plane view of the particles. The SEM analysis of uncoated particles was not possible due to the non-conducting nature of polyacrylate plastic.

The SEM images of the particles and the magnified views of the surfaces depicting the roughness features and edges of the particles are shown in Fig. 3.3. An estimate from the magnified views indicate that roughness feature dimensions were of the order of tens of micrometers. The magnified micrographs also indicate that the roughness on flat surfaces was generally less than on curved surfaces. The roughness contributes to both the deviation of the experimental force-position plots from theoretically calculated curves, as well as the deviation of the actual contact angles from the macroscopically measured contact angles.

### 3.4.4 High-speed Video Capture of Interface Pinning on Model Particles

To visualize the position and configuration of the air-water interface at the particles during the process of immersion, we used a high-speed video camera (MotionBLITZ Cube 3, Mikrotron GmbH, Unterschleissheim, Germany)

equipped with a 50 mm, f/1.4 lens (Nikon Inc., Melville, NY). We shot  $320 \times 160$  pixel videos at 1000 frames/sec, with the camera attached to a standard laptop computer over a gigabit ethernet link. The lighting for the video photography was provided by a 1000W halogen flood-lamp placed 15 cm away from the sample platform.

### 3.4.5 Numerical Calculation of Capillary Forces

The capillary rise,  $z_c$ , was calculated as a function of position along the  $z$ -direction for each of the nine model particles according to Equation 3.1. As the air-water interface is advancing during the immersion of the particles, we used the advancing contact angle ( $151^\circ$ ) for the numerical calculations. The calculated capillary rise was then used to determine the capillary force (sum of surface tension and pressure forces) experienced by the particle at that position. The total calculated force (capillary and buoyancy forces) was then plotted against the air-water interface position to obtain a theoretical force-position curve.

For the particles with a fixed cross-section (cylinder, hexagonal cylinder, cube), which had an abrupt edge at the top, the air-water interface gets pinned at the edge. We calculated the capillary forces under conditions of pinning using the Gibbs' inequality (Equation 3.3). The wedge angle for all three fixed cross-section particles was  $90^\circ$ . The pinning distance,  $z_{pin}$ , was obtained as the difference between the experimental distance over which the particle and the air-water interface were found to interact, and the experimentally measured  $z$ -axis height of the particle (Table 3.2). We then calculated the force-position curve for angular increments over the total pinning distance.

## 3.5 Results and Discussion

### 3.5.1 Results Expected from Theory

When a force-position curve is determined with the process tensiometer, the tensiometer microbalance measures the total force on the particle, i.e., the sum of the surface tension force, the pressure force, and the buoyancy force. Only the vertical component of the net force is registered, and we define downward forces as positive, and upward forces as negative. The three categories of model particles are expected to interact differently with the air-water interface. Different stages of the position of the air-water interface on the particles are illustrated in Fig. 3.2. In the following paragraphs, we discuss the shapes of the force-position curves that are expected from theory.

*Particles with rounded cross-section.* The particles with rounded cross-sections are expected to have a smooth and continuously varying capillary force as a function of distance. The vertical component of the capillary force, while varying continuously, will change direction from a downward to an upward force due to

the change of the interface curvature from concave to convex, caused by the fixed contact angle on the particle surface (Fig. 3.2a).

At the initial contact, when the particle first touches the air-water interface, a positive, downward force is registered, due to a surface tension force and a pressure force. As the interface moves upward, the downward capillary force increases, but soon reaches a maximum, after which the vertical component of the capillary force decreases more and more because the surface tension component of the capillary force starts pointing in horizontal direction. For a particle with  $90^\circ$  contact angle, the vertical component of the capillary force is zero exactly when the air-water interface is at the equatorial plane. As the air-water interface contact line passes the equatorial plane, the capillary force changes direction. For our experimental particles (contact angle  $\theta=151^\circ$ ), this change in direction of the vertical component of the capillary force is expected to occur at around  $29^\circ$  latitude below the equator. As the air-water interface contact line continues to move upwards, the particle begins to experience an upward pointing (negative) capillary force. Due to symmetry, the now upward pointing capillary force passes through a negative maximum value, before the force reduces again because of the reduction in the length of the contact line (perimeter).

The force-position curve shows the net vertical force on the particle as a function of position of the air-water interface. The position is measured as the distance of the air-water interface from the bottom boundary of the particle. The contact line would ultimately reduce to a very small perimeter at the top of the particle (Fig. 3.2a) causing the surface tension force and the distortion of the air-water interface due to the contact line to be small, which cause the pressure force to be proportionately small. At that point, the largest force registered by the tensiometer is the negative and upward pointing buoyancy force. For a smooth, round particle we do not expect any pinning to occur. This behavior of the force will give rise to a sinusoidal force-position curve as schematically depicted in Fig. 3.5.

*Particles with fixed cross-section.* The particles with fixed cross sections are expected to have a constant value of both the surface tension and the pressure forces (total capillary force), irrespective of the position of the air-water interface line, because the shape of the air-water interface remains identical as the interface moves along the fixed cross section (Fig. 3.2b). The buoyancy force is expected to increase progressively. The combined value of the force registered on the tensiometer should, thus, be progressively increasing (upward pointing) with the increase being due to buoyancy force only (Fig. 3.5).

At the edges of the fixed cross-section particles, we can expect interfacial pinning (Fig. 3.2b). Following the Gibbs' inequality, the contact angle will increase at the edges until the interface slips off. At the bottom of the particle the interface will slip off onto the vertical side of the particle, at the top of the particle the interface will snap-off from the particle thus immersing the whole particle

into the water. So, we expect the pinning phenomena to be similar at both the bottom and the top edges, the slopes of the force position curve should be similar for both edges, but different from when the interface is sliding along the vertical face of the particle. Thus, we expect a three segment form of the force-position curve for the particles of fixed cross-section (Fig. 3.5). In the first segment, we have a constantly increasing, negative, upward force as long as the interface is pinned to the bottom. This is followed by a segment with an increasing, negative upward force, due to the fixed contact line and increasing buoyancy force. Finally, when the air-water interface reaches the top edge of the particle, it gets pinned, and the negative upward force increases again, similar to the case with the bottom pinning. The final expected feature is the snap-off of the interface from the top edge of the particle.

*Particles with tapered cross-section.* The particles with tapered cross-sections are expected to have a constantly decreasing value of both the surface tension and the pressure forces, because the cross-sectional area and the length of the contact line are continuously decreasing as we proceed from the broad bottom of the particles to their pointed top (Fig. 3.2c). The buoyancy force is expected to progressively increase as the particle is immersed in the water, however, the rate of increase of the buoyancy force should slow down as the particle tapers off at the top. The overall shape of the force-position curve should have two segments (Fig. 3.5). The first segment is an increasing, upward pointing, negative force due to an increasing surface tension force and a pressure force as long as the air-water interface remains pinned to the bottom edge. The second segment, when the interface moves along the side walls of the particle, is also negative and upward pointing, but the negative force becomes continuously smaller (i.e., the force-position curve shows a positive slope) as the cross-section of the particle decreases. The plot ends at the negative value of the buoyancy force of the totally immersed particle. No pinning is expected at the top because the tapered particles have a pointed end; i.e., ending in a point for the cone, square pyramid, and the tetrahedron, or a line for the trigonal prism (tent-shaped).

### 3.5.2 Observations from High-Speed Videos

The videos played in slow motion provide interesting insights into the interaction of the air-water interface with the particles, illustrating the locations of pinning due to sharp edges as well as roughnesses originating from the printing process (see supporting information). The videos show the depression of the air-water interface due to the pinning effect and the curvature of the interface at various positions along the surface of the particle. Details are discussed in the Supporting Information.



### 3.5.3 Description of Experimentally Obtained Force-Position Curves

Fig. 3.6 shows a typical experimental force-position curve measured on the process tensiometer for an ellipsoidal particle. There is a pronounced downward (i.e., positive) force at the onset indicated by a spike in the plot. This feature is due to the snap-in of the air-water interface at the juncture of the steel hook and the bottom of the model particles (Fig. 4.1). This is an experimental artifact due to the presence of the steel hook, which alters the initial shape of the force-position curve and the starting point of the subsequent force-position curve due to the particle interacting with the air-water interface. However, the remainder of the points on the plot are not affected by this artifact and follow the expected curve from a freely suspended particle (without the hook). Fig. 3.6 also shows a constant force at the end of the curve, which indicates that the particle is totally immersed in water. The constant force registered at the end is the buoyancy force, which manifests as a negative, upward pointing force.

For all the following experimental force-position curves, to make the comparisons independent of the variations due to the mounting of the hook, we removed the spike at the onset and set this position as the zero position. We also removed the part at the end where only the buoyancy force is being measured. We only compare the curves during the immersion of the particles.

### 3.5.4 Reconstruction and Interpretation of Force-Position Curves

Fig. 3.7 shows the experimentally obtained and theoretically calculated force-position curves for all nine particles. Table 3.2 lists the maximum deflection of the air-water interface due to pinning as well as the maximum experimental and theoretical forces experienced by the particles as determined from the force-position curves. In the following, we discuss the data for each category of particles.

*Particles with round cross-sections.* The experimental force-position curves of the spheroidal particles (sphere and ellipsoid) have a smooth, rounded shape, as is expected from theory (Fig. 3.7a-b). The experimental curves differ in two key aspects from the theoretically calculated curves. First, the round shape of the curve at the onset are obscured by the snap-in phenomena and artifacts due to the presence of the hook. Second, the experimental curves extends over a longer distance than the actual  $z$ -axis dimension of the particle. This extension is due to (1) snap-in of the interface at the bottom and associated pinning due to attachment of the hook, (2) local pinning of the interface on roughness features on the particle surface, and (3) the pinning of the interface at the top of the particle, again due to surface roughness. Further support of these explanations is provided when we scale the theoretical curves over the same distance as the experimental curves. The scaled theoretical curves, especially for the ellipsoid,

match the experimental curves well (Fig. 3.9, Supporting Information). For the spherical particle, the shape of the curve is similar, but the magnitude of the forces calculated using theory are lower than those observed experimentally.

The difference between the total distance of interaction of the particle with the air-water interface and its actual height is denoted by its pinning distance,  $z_{pin}$  (Table 3.2). The distance  $z_{pin}$  is the cumulative deflection of the air-water interface from its flat, undisturbed surface. The theoretically calculated forces at corresponding positions are in best agreement with experimental values for the ellipsoid, as reported previously in *Chatterjee et al.* [2012], however, the flatter shape of the ellipsoid also causes a more pronounced pinning than compared to the spherical particle, as can be seen by the increased ratio of  $z_{pin}/z_{max}$ . The magnitude of the forces calculated theoretically are, in general, smaller than the experimental forces due to the absence of local pinning considered in the calculations.

*Particles with fixed cross-sections.* The experimental force-position curves for the particles with a fixed cross-sectional area (Fig. 3.7c-e) show the expected three segment form. The distinct slope changes between the segments in the theoretical curves are, however, less pronounced in the experimentally observed force-position curves. This is because the particles did not have perfectly sharp edges, and the interface crept around the edges of the particles. This creeping of the interface around the sharp edges could be observed in the high-speed videos (see supporting information). The creeping phenomena around the edge caused the slope of the experimental force-position curve to change more gradually than that in the theoretical curve. Due to the creeping of the interface over the top edge, the snap-off from the top actually occurs from the top face rather than from the top edge, thus causing the experimental maximum force to be less than the theoretical maximum force (Fig. 3.7c-e).

*Particles with tapered cross-section.* The experimental force-position curves for the particles with a tapered cross-section (Fig. 3.7f-i) show a shape which reflects the progressively decreasing cross-section of the particle interacting with the air-water interface, as the interface line moves towards the top of the particle. The eventual vanishing of the capillary force is apparent in the cone, the square pyramid, and the tetrahedron, all of which show a lack of interface pinning at the top. The square tent which has a straight top edge shows a small pinning (Fig. 3.7i). The general trend in the force-position curves can be explained by the progressive decrease in both the surface tension force, due to decreasing length of the contact line, and the pressure force, due to decreasing area of the cross-section. The rate of increase of the buoyancy force also slows down as the particle tapers towards the top; therefore, the total upward force gradually reduces to the final baseline value of the buoyancy force. The theoretical reconstructions of the force-position curves follow a similar trend as the experimental curves.

The quantitation of the force magnitude is, however, not exact due to the local pinning and change in contact angles as discussed above (Table 3.2).

### 3.5.5 Maximum Capillary Forces and Snap-off Forces

Except for the cone, square-pyramid and tetrahedron (Fig. 3.7f-h), the experimental force-position curves for all other particles show a pinning effect and snap-off of the air-water interface at the top. This snap-off of the interface is manifested as a sharp rise in the force-position curve and is due to the sudden loss of the surface-tension and pressure force components.

A comparison of the force-position curves of the three classes of particles shows that the snap-off is the most abrupt for the particles with fixed cross-section, followed by that in the rounded particles. The particles of tapered cross-section show an almost complete lack of pinning at the top edge. The particles have different snap-off forces and maximum capillary forces on account of their shape.

Table 3.2 lists the maximum, upward (negative) forces experienced by each model particle as well as the snap-off forces. The data show that fixed cross-section and sharp-edged particles experience the largest forces. Particles with tapered cross-sections, however, show smaller maximum capillary forces than even the rounded cross-section particles, a result of their smaller contact lines and cross-sections.

The theoretical maximum force is best estimated for the ellipsoid. The theoretical estimate of the maximum force for the sphere is lower than the experimental value, likely because we did not take into consideration the local pinning of the interface. For all other particles, except the trigonal prism, the theoretically estimated maximum force is larger than the experimentally measured maximum force. This is because for the experimental curves, the air-water interface crept around the edges of the particles, and thus, the magnitude of the forces due to interface pinning was reduced. However, for all the particles, the interaction distance along the  $z$ -axis is longer for the experimental curves ( $z_{pin}/z_{max} > 0$ ), which reinforces the importance of localized pinning effects due to roughness of the surfaces on the capillary forces (Table 3.2).

## 3.6 Implications









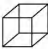
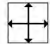



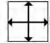



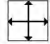
Capillary forces acting on particles at the air-water interface have been found to exceed DLVO and gravity forces [Shang *et al.*, 2008; Scheludko *et al.*, 1976; Preuss and Butt, 1998a; Shang *et al.*, 2009], and the smaller the particles, the more dominant the capillary forces become. Moving air-water interfaces have been implicated in the detachment of colloidal particles from solid surfaces at the pore scale [Leenaars and O'Brien, 1989; Noordmans *et al.*, 1997; Sharma *et al.*, 2008a; Aramrak *et al.*, 2011] as well as at the porous medium scale [Zhuang

*et al.*, 2007; *Sharma et al.*, 2008a; *Cheng and Sayers*, 2009; *Sayers and Lenhart*, 2003; *Sayers et al.*, 2003]. Thus, capillary forces play an important role in colloid mobilization from matrices, like soils and sediments. Situations of moving air-water interfaces in soils arise during water drainage and infiltration events.

The force-position curves for particles interacting with moving air-water interfaces show a variety of features, dictated by the particle shape, surface roughness, and particle orientation. Pertinent features are the pinning and creeping of air-water interfaces over sharp edges, as well as the pinning of interfaces at surface roughnesses and the associated increase of contact angles. The characteristics of the force-position curves allows us to deduce the magnitude and dynamics of the capillary forces acting on a particle. Our studies indicate that force-position curves can be broadly classified into three different categories based on shape (in direction of the air-water interface movement): (1) round particles, (2) fixed cross-section particles, and (3) tapered particles. Among these particle shapes, tapered particles are least likely to be dislodged by a moving air-water interface, whereas particles with edges, or particles with surface roughness get most readily mobilized.

### 3.7 Tables and Figures

Table 3.1: Characteristics of model particles.

shape	schematic		length	width	height
	shape	top-view*	(mm)	(mm)	(mm)
ROUNDED CROSS-SECTION					
sphere			4.95 (diameter)		
ellipsoid			5.56	4.89	2.57
FIXED CROSS-SECTION					
cylinder			5.02 (radius)	5.04	
hexagonal cylinder			4.97	4.35	5.14
cube			5.20	5.04	5.04
TAPERED CROSS-SECTION					
cone			4.87 (radius)	5.04	
square pyramid			4.92	4.82	3.67
tetrahedron			4.87	4.22	3.98
trigonal prism			5.00	4.90	4.28

\* arrows indicate how length and width were measured.

Table 3.2: Pinning distances and maximum capillary forces (experimental and theoretical). Negative forces indicate upward forces, that is, forces pointing in direction from the water to the air phase.

shape	dimensions			capillary force ( $\mu\text{N}$ )		
	(mm)		ratio	experimental		theoretical
	$z_{\text{max}}^*$	$z_{\text{pin}}^\dagger$	$\frac{z_{\text{pin}}}{z_{\text{max}}}$	$f_{\text{max}}$	$\Delta f_{\text{snap-off}}^\ddagger$	$f_{\text{max}}$
sphere	4.95	1.50	0.30	-1150	289	-672
ellipsoid	2.57	1.52	0.59	-1055	480	-1008
cylinder	5.04	2.00	0.40	-1751	689	-1927
hexagonal cylinder	5.14	2.81	0.55	-1701	607	-1780
cube	5.04	3.64	0.72	-2466	820	-2959
cone	5.04	0.58	0.11	-594	16	-679
square pyramid	3.67	1.44	0.39	-967	30	-680
tetrahedron	3.98	0.63	0.16	-437	3	-504
trigonal prism	4.28	1.83	0.43	-956	268	-841

\*  $z_{\text{max}}$  = height of particle along  $z$ -axis measured using a pair of calipers,

$^\dagger z_{\text{pin}}$  = total pinning distance along  $z$ -axis, measured from experimental force-position curves,

$^\ddagger \Delta f_{\text{snap-off}}$  = force change due to the snapping off of the air-water interface leading to full immersion of the particle in water.

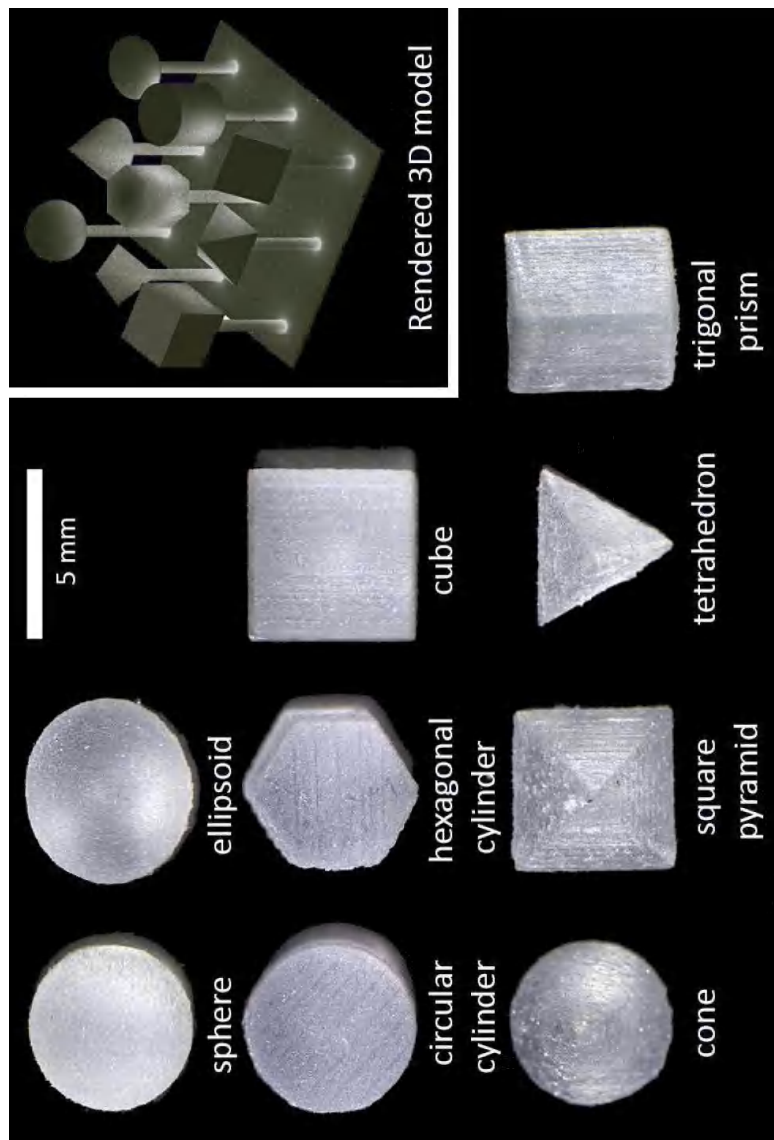


Figure 3.1: Dissection scope images of the nine model particles (view from the top). Inset: 3D rendering of the model used for 3D printing, including the attachment sticks and base-plate.

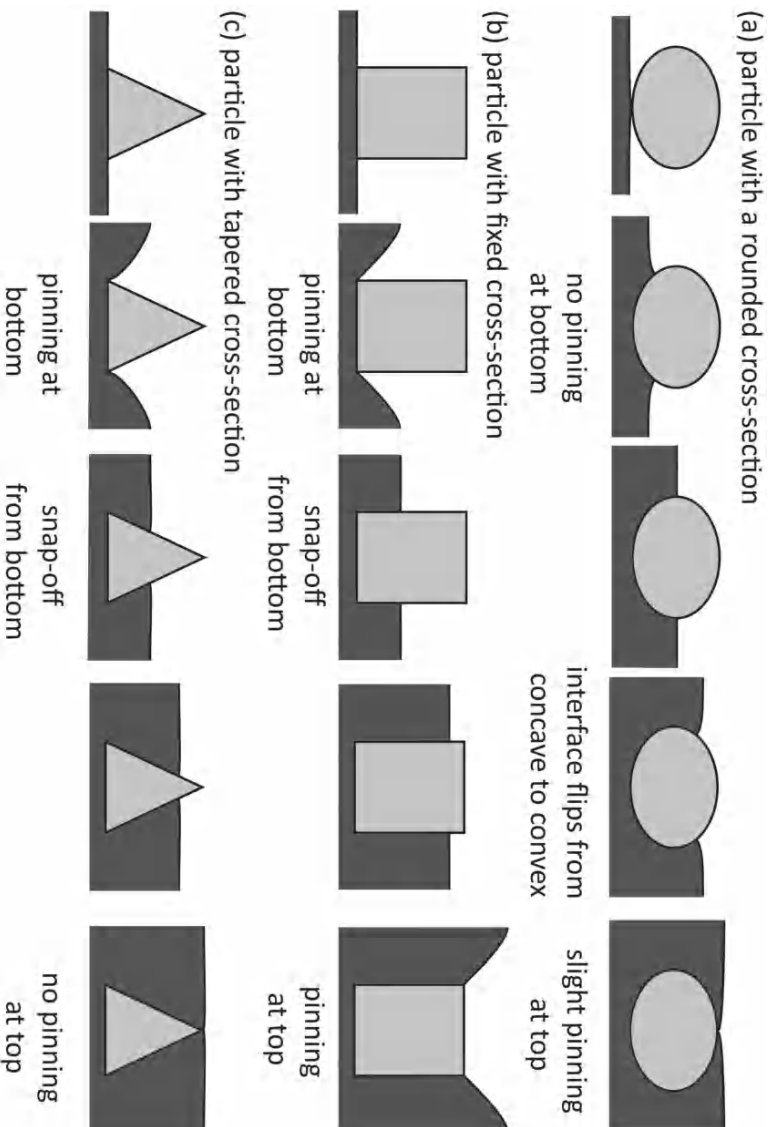


Figure 3.2: Schematic diagram of particle cross-sections and air-water interface interaction for different positions of air-water interface on the particles. The air-water interface moves from bottom to top in the schematic diagrams (from left to right). The schematics depict an advancing contact angle of  $90^\circ$ .



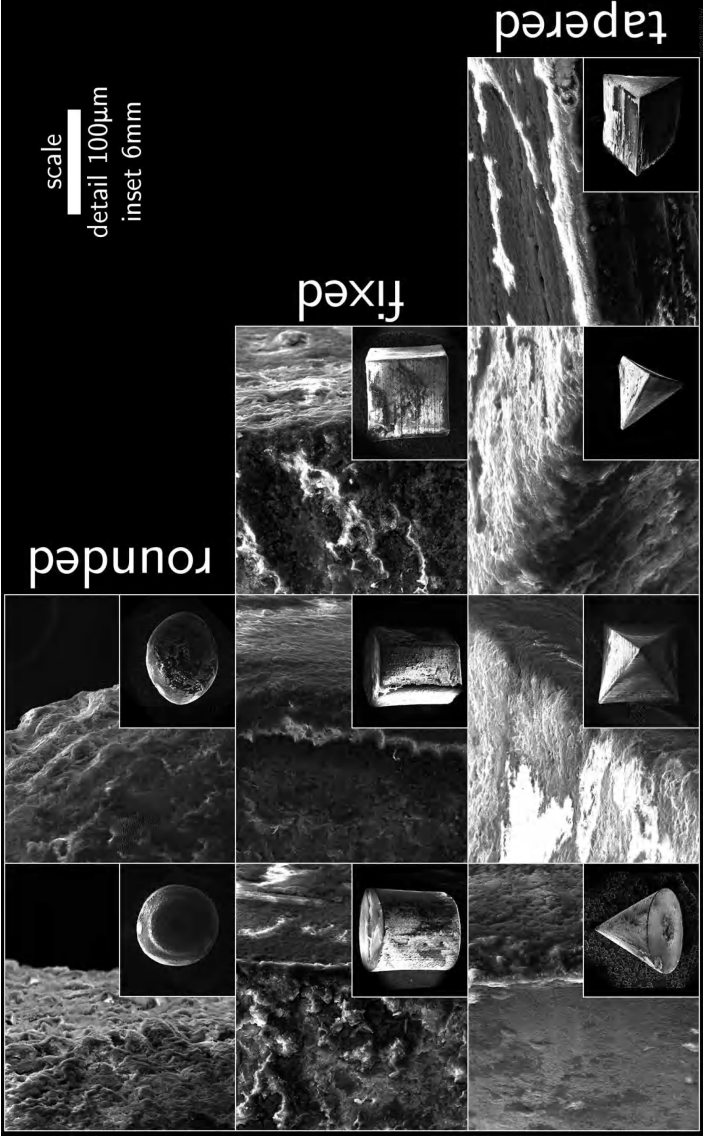


Figure 3.3: Scanning electron micrographs of the surface of the 3D printed particles. The detailed views are a 60 $\times$  magnification of the particle overview images shown in the insets. The detailed views are taken on the edges of the particles to give an understanding of the size of roughness features.

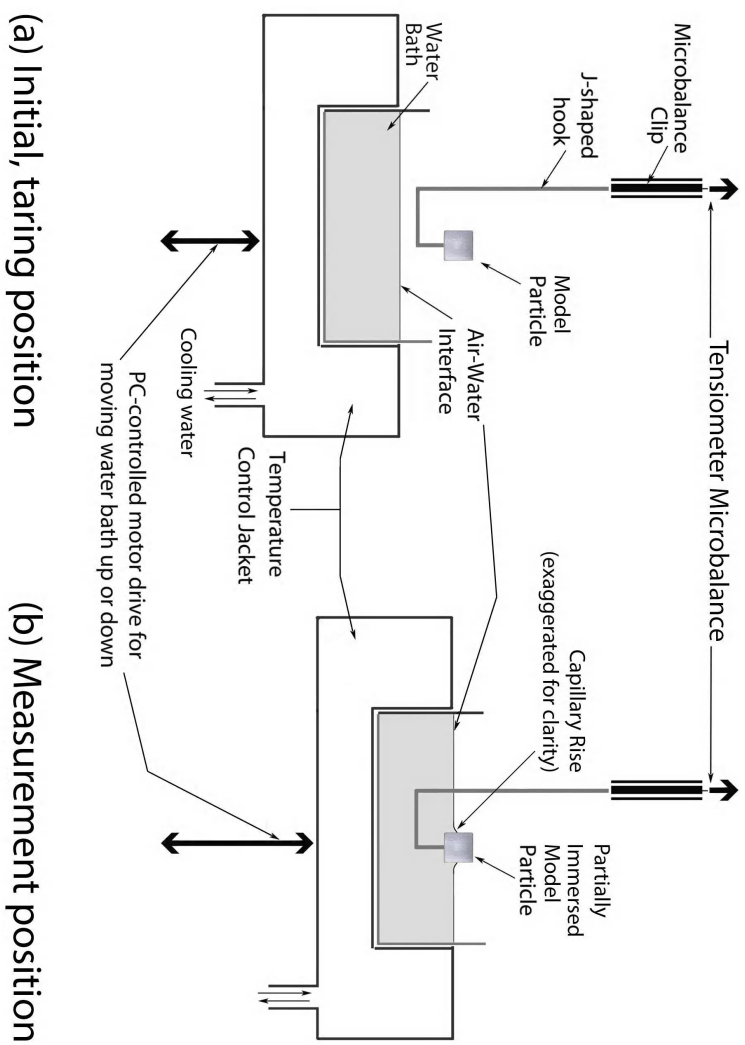


Figure 3.4: Schematic of experimental set-up for force-position curve measurements using a tensiometer. (a) Initial, taring position with particle and hook in air (b) Measurement position with particle and hook, both partially immersed in water, and interacting with the air-water interface.

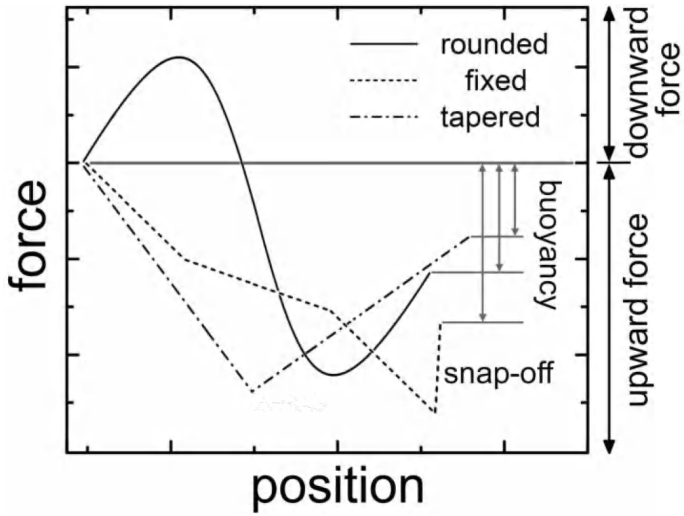


Figure 3.5: Schematic of force-position curves during immersion for model particles with different categories of cross-sections. The vertical double-arrows inside the figure indicate the buoyancy force for the completely immersed particles. Force and position axes have arbitrary units.

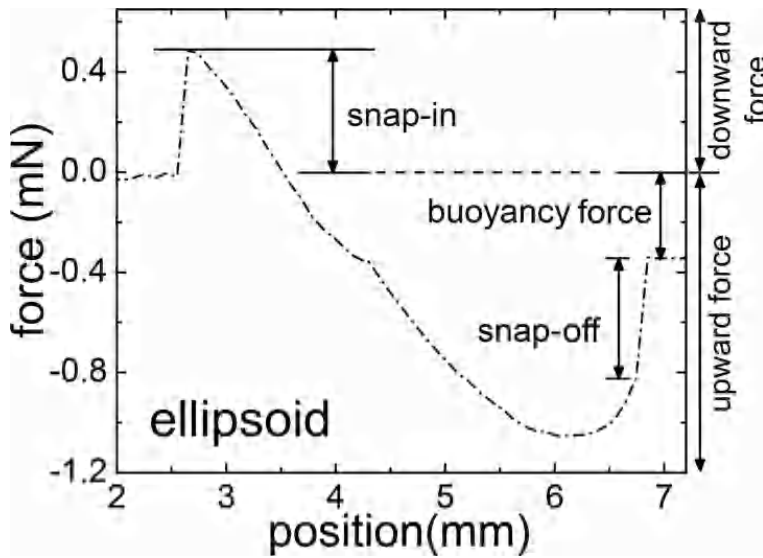


Figure 3.6: A typical experimental force-position curve, measured with a processor tensiometer, obtained for an ellipsoidal particle. Note the presence of a snap-off even though a snap-off is not expected for a particle of rounded cross-section. The advancing contact angle for the particle is  $\theta = 151^\circ \pm 2^\circ$ .

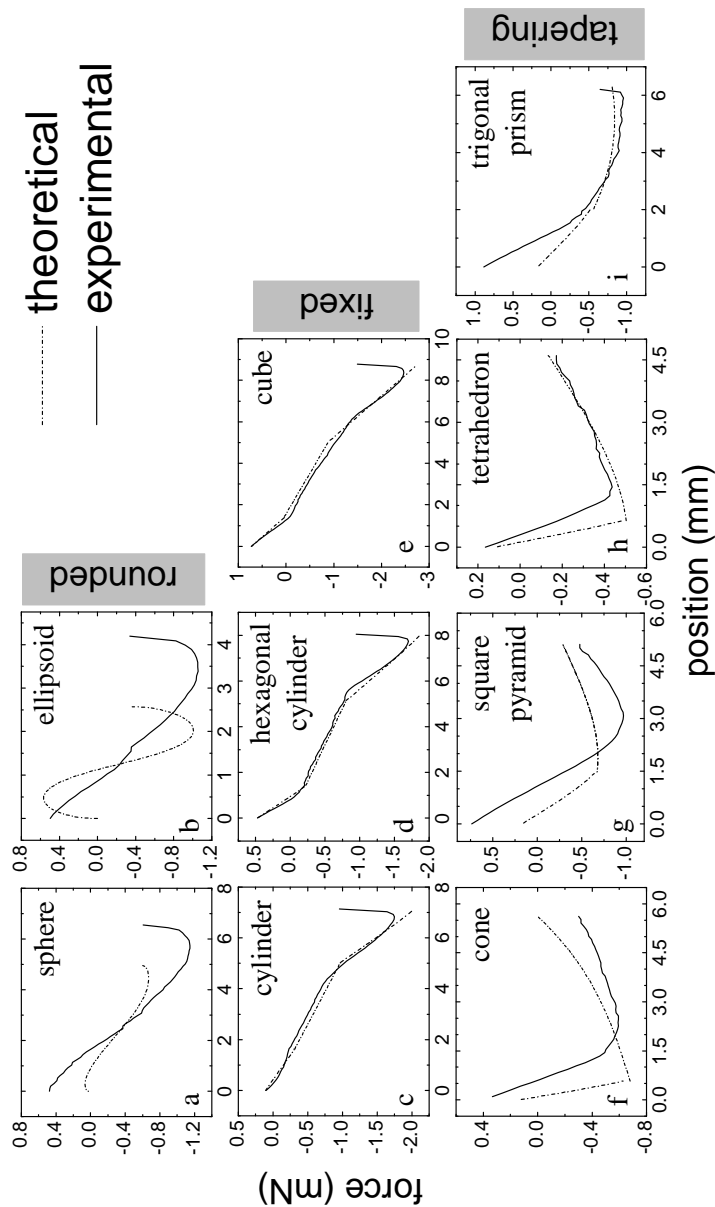


Figure 3.7: Comparison of experimental and theoretically reconstructed force-position curves during immersion for nine model particles. The advancing contact angle for the particles is  $\theta = 151^\circ \pm 2^\circ$ .

## 3.8 Appendix 3A: Supporting Information

Supporting information contains:

1. Details on the capture of the high-speed videos of particles being immersed into an air-water interface. Videos are available in MP4 format.
2. Figure showing comparison of experimental and scaled theoretical force-position curves during immersion for spherical and ellipsoidal particles.

---

This section was accepted for publication as supporting information to the journal article: Chatterjee, N., and M. Flury, (2013), Effect of particle shape on capillary forces acting on particles at an air-water interface, *Langmuir*, **29**, (in press).

### 3.8.1 Method for High-speed Videography

High-speed videos were taken with a MotionBlitz Cube 3 high-speed camera (Mikrotron GmbH, Unterschleissheim, Germany) and a Nikon 50 mm lens. Lighting was provided by a standard 1 kW floodlamp placed 15 cm away from the platform and water bath in which the particle was being immersed. The camera was attached to a laptop running Windows 7 equipped with a Gigabit ethernet port using a standard Cat5 LAN cable. The camera management and frame-capture software supplied by Mikrotron (MotionBlitz Director 2) was used to capture and store the videos.

The original videos were taken at 1000 frames/second at a frame size of  $320 \times 160$  pixels. The MotionBlitz software saved the raw video footage as XVID encoded AVI (audio video interleave) files. The videos were later edited (time and frame cropping) using HandBrake version 0.98 and saved as 100 frames/second, x264 encoded MP4 files. The videos available online for viewing were set up to play at a speed one-tenth of the speed at which they were taken. This enables us to view the air-water interface interacting with the particle in slow-motion. The frames were cropped to  $214 \times 160$  pixels.

### 3.8.2 Discussion

The videos allow us to view a number of key events about the interaction of the air-water interface with the particles.

*Particles with rounded cross-section.* The videos show the abrupt force change during the snap-in of the air-water interface. This abrupt movement of the interface manifests itself as large spike in the force-position curve, and is visually seen as being followed by large-amplitude undulations on the air-water interface. Another key feature for particles of rounded cross-section is the change in direction of the direction of curvature of the interface. For the spherical particle this occurs at a position of the interface below the equatorial plane. For the flatter ellipsoidal particle this change in direction of curvature of the interface is past the position of the equatorial plane.

*Particles with fixed cross-section.* Similar to the videos of the round particles, the snap-in of the air-water interface with the bottom of the particles is observable for particles with fixed cross-section. After the snap-in, we observe a continuously larger diameter depression of the air-water interface being created as the particles move down with the air-water interface remaining pinned at the bottom edge. When the particles are less than half immersed in the water the interface depression becomes smaller and thereafter remains at a fixed size indicating sliding of the air-water interface line along the vertical walls of the particles. The depression size starts increasing again when the particles are completely underneath the surface of the undisturbed air-water interface. Near the end of the video, we observe a rapid reduction in the size of depression formed in the air-water interface as the contact-line creeps across the top of the particle,

before eventually snapping off of from the top face of the particles. The snap-off is also followed by large amplitude waves on the rapidly equilibrating air-water interface.

*Particles with tapered cross-section.* The particles with a tapered shape also interface snap-in at the bottom edge of the particles, and the subsequent pinning at the bottom edge. However, after the air-water interface snaps-off from the bottom edge of the tapered particles, the size of the depression formed decreases continuously. There is almost no observable pinning at the top, as is expected for such particles. The trigonal prism (tent-shape), however, does shows some pinning at its top edge.

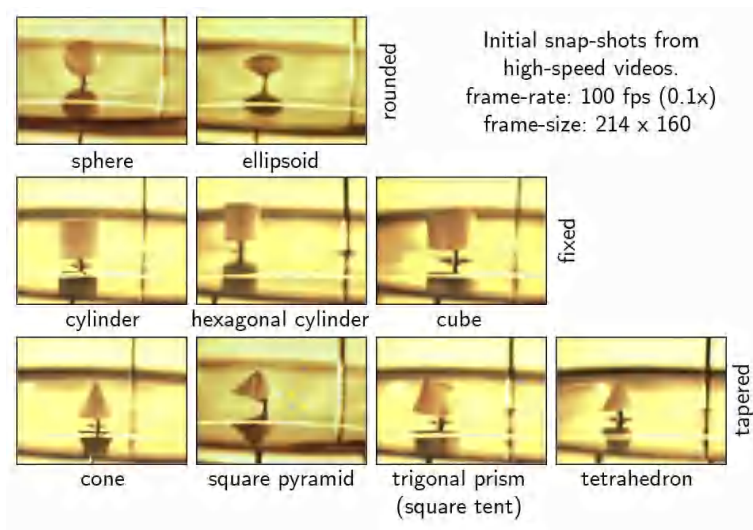


Figure 3.8: Snap-shots of particles of different cross-sections prior to snap-in of the air-water interface.



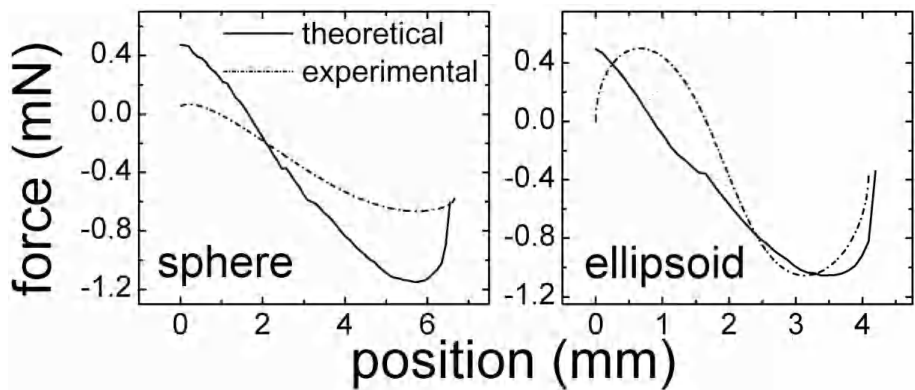


Figure 3.9: Comparison of experimental and scaled theoretical force-position curves during immersion for spherical and ellipsoidal particles. The advancing contact angle for the particles is  $\theta = 151^\circ \pm 2^\circ$ .



# Chapter 4

## Numerical Simulation of Capillary Forces Acting on Subsurface Particles at Air-Water Interfaces

### 4.1 Abstract

Moving air-water interfaces occur in unsaturated porous media like soils and sediments when water infiltrates or drains during precipitation or irrigation and subsequent redistribution events. Moving air-water interfaces can dislodge colloidal particles from stationary substrates like soil aggregates. The mobilization of colloidal particles is due to the capillary forces exerted by the moving air-water interface on the particles. The magnitude of such forces is dictated by the particle shape, the orientation, and the surface properties like roughness and contact angles. This study looks at capillary forces on mm-scale particles from an experimental and a theoretical standpoint. The experimental forces were measured using tensiometry, and the theoretical forces were calculated based on surface reconstructions done using scanning electron microscopy, on two sediment particles (basalt and quartz). We measured capillary forces at different positions of the air-water interface along the particle surface to generate an experimental force-position curve. Surface reconstruction using triangular meshes at three different resolutions was done, followed by subsequent generation of theoretical force-position curves. The results indicate that theoretical surface reconstructions provides a close estimate of the maximum capillary forces on a mm-scale sediment particle. However, results indicate that even though somewhat crude surface reconstructions (e.g. mesh triangle edges  $\approx 10\%$  of particle root-mean-square radii) are capable of estimating the maximum capillary forces, the local pinning cannot be predicted.

## 4.2 Introduction

Particles at an air-water interface give rise to a three-phase interface. The presence of three phases with different surface energies causes the non-rigid fluid phases (gas and liquid) to equilibrate at a particular conformation at the three-phase boundary dictated by a particular interfacial angle of interaction, called the contact angle. The curvature of the air-water interface gives rise to height differentials of the liquid phase which results in pressure differences. The combination of the surface tension force and the pressure force is called the capillary force. Capillary forces have been reported to be of particular importance at moving air-water interfaces in porous media, and may exceed other interfacial forces like DLVO (electrostatic) forces [Scheludko *et al.*, 1976; Preuss and Butt, 1998a; Sharma *et al.*, 2008b; Shang *et al.*, 2009], and can lead to attachment or detachment of lighter particles from stationary solid surfaces [Leenaars and O'Brien, 1989; Noordmans *et al.*, 1997; Gomez-Suarez *et al.*, 1999b; Shang *et al.*, 2008; Aramrak *et al.*, 2011; Lazouskaya *et al.*, 2011; Aramrak *et al.*, 2013].

The quantitation of capillary forces due to air-water interfaces is important in understanding of a number of natural physical phenomena [de Gennes *et al.*, 2004]. For example, capillary forces on small particles in a porous medium like unsaturated soil is an important area of investigation, in part due to the role of such forces in mobilization of nutrients and contaminants [McCarthy and Zachara, 1989]. Capillary forces are responsible for both attachment [Noordmans *et al.*, 1997; Wan and Tokunaga, 1997; Veerapaneni *et al.*, 2000] and detachment and mobilization [Shang *et al.*, 2008; Zhuang *et al.*, 2007; Sharma *et al.*, 2008a; Cheng and Saiers, 2009] of colloidal particles to and from solid substrate surfaces. The preferential attachment of particles to the air-water interface has also been used in industrial processes, for example in cleaning semiconductor wafers [Leenaars and O'Brien, 1989; Noordmans *et al.*, 1997; Gomez-Suarez *et al.*, 1999b; Gomez-Suarez *et al.*, 1999a].

Force tensiometry has been used as a method of measuring the capillary force on mesoscale and macroscale particles [Shang *et al.*, 2008; Zhang *et al.*, 1996; Zhang *et al.*, 1997; Chatterjee *et al.*, 2012]. The classical methods of measuring capillary forces, using probes like the Wilhelmy plate, the du Noüy ring, and spherical or spheroidal beads [Zhang *et al.*, 1996; Gunde *et al.*, 1995; Ecke *et al.*, 1999] are all based on force tensiometry. In the past couple of decades, with the advent of microscopic manipulation methods like atomic force microscopy, capillary forces on microscopic particles, mostly of spherical shapes have also been reported [Preuss and Butt, 1998a; Preuss and Butt, 1998b; Gillies *et al.*, 2005; Englert *et al.*, 2009; Yamamoto *et al.*, 2010]. Recently, measurements have also focused on measuring capillary forces on irregularly shaped natural sediment particles [Shang *et al.*, 2008; Chatterjee *et al.*, 2012] and particles of standard geometric shapes [Shang *et al.*, 2009; Singh and Joseph, 2005; Chatterjee and Flury, 2013].

Theoretical calculations of capillary forces are done by numerically solving

the Young-Laplace equation. The numerical solution requires putting in place the appropriate boundary conditions to analytically solve the equation. Numerical solution of capillary forces on spherical particles have been reported by several authors [Zhang *et al.*, 1996; Zhang *et al.*, 1997; Ecke *et al.*, 1999; Princen, 1969]. Recent studies have also investigated numerical solutions for axisymmetric, but non-spherical particles [Chatterjee *et al.*, 2012; Singh and Joseph, 2005; Hesla and Joseph, 2004].

Measurements on irregularly shaped particles have shown that the overall shape and surface roughness of the particles have a major effect on the magnitude of the capillary forces that arise out of the interaction with a moving air-water interface. Irregularly shaped particles have sharp edges and corners formed due to mechanical and chemical weathering processes on mineral matter. Such surface features and morphologies lead to air-water interfaces to get pinned to, and subsequently suddenly snap-off from, the solid particles. Such phenomena cause irregular particles to experience unbalanced and large capillary force changes. Pinning of the air-water interface to features on the particle surface cause a pin-slip behavior of the interface rather than a smooth movement.

In previously reported studies by our group [Shang *et al.*, 2009; Shang *et al.*, 2008; Chatterjee *et al.*, 2012; Chatterjee and Flury, 2013], we have reported capillary force measurements using tensiometry on both regularly shaped particles and on irregularly shaped particles. In this study, we describe the theoretical reconstruction of the typical force-position curves obtained from a process tensiometer, using a surface reconstruction, for natural, millimeter-scale sediment particles. We investigate how the calculated position variation of the capillary force, the maximum capillary force, and the shape of the force-position curve experienced by the sediment particles depend on the spatial resolution of the surface reconstruction.

## 4.3 Theory

### 4.3.1 Capillary Rise and Total Force on a particle at an Air-Water Interface

The capillary rise,  $h$ , at a Wilhelmy plate is given by:

$$h = \sqrt{(1 - \sin \theta) \frac{2\gamma}{\rho g}} \quad (4.1)$$

where,  $\theta$  is the contact angle at the three-phase interface,  $\gamma$  the surface tension of the liquid-gas interface,  $\rho$  the density of the liquid phase, and  $g$  the acceleration due to gravity.

If we consider an irregular particle as a surface constructed out of numerous plate-like, triangular faces, then we can use the formula for the capillary rise, as

above to calculate the capillary force on an individual segment of the contact line. When we consider the sum of all these contact line segments, at any particular  $z$ -axis position of the interface along on a suspended irregular particle, we can calculate the total surface tension force due to the contact line. The total force,  $f$ , acting on a particle at an air-water interface is given by:

$$f = f_s + f_p + f_b = l\gamma + A\rho gh + \rho gV_i \quad (4.2)$$

where,  $f_p$  is the pressure force due to the capillary rise and interface curvature,  $f_s$  is the surface tension force at the interface, and  $f_b$  is the buoyancy force due to the portion of the particle immersed into the liquid phase,  $A$  is the cross-sectional area of the particle interacting with the air-water (gas-liquid) interface,  $l$  is the length of the contact line at the three-phase interface,  $\gamma$  is the surface tension of the air-water (liquid-gas) interface, and  $V_i$  the volume of particle immersed in liquid phase at a given position of the air-water interface on the surface of the particle.

### 4.3.2 Gibbs' Inequality and Interfacial Pinning

For particles with smooth surfaces, a moving air-water interface adjusts to the equilibrium position with the contact angle at an equilibrium value particular for that three-phase interface. When the moving air-water interface interacts with a rough or discontinuous surface with edges, it may get pinned to the edge, resulting in a non-equilibrium situation. Such non-equilibrium conditions may persist even when the bulk of the moving air-water interface moves to a newer position. This causes the interface to get distorted at the location of the edge on the particle resulting in a non-equilibrium contact angle. In such cases, the new contact angle can be described by the Gibbs' extension to the Young Equation [Singh and Joseph, 2005]:

$$\theta_0 < \theta < 180^\circ - \alpha + \theta_0 \quad (4.3)$$

where  $\theta_0$  is the equilibrium contact angle for a smooth solid surface interacting with an air-water interface,  $\theta$  is the non-equilibrium contact angle on the same three-phase interface with the air-water interface pinned on an edge on the solid phase, and  $\alpha$  is the wedge angle at the edge measured through the solid phase. The relationship dictates that the non-equilibrium contact angle may exceed the equilibrium contact angle up to a critical value. This distortion of the contact angle causes the capillary forces to increase. When the non-equilibrium contact angle reaches the critical value, the air-water interface contact line will snap off from the edge on the solid phase and form again at a new position. However, the inequality only gives the limits of the non-equilibrium contact angle, the air-water interface may snap off before  $\theta$  reaches the critical value. It thus only provides an approximate indication of how much the capillary force can change.

## 4.4 Materials and Methods

### 4.4.1 Capillary Force Measurements

The capillary forces between the particles and an upward moving air-water interface were measured with a tensiometer (Process Tensiometer K100, Krüss GmbH, Hamburg, Germany). The smallest weight the microbalance can measure is 0.02 mg corresponding to a force of  $0.196 \mu\text{N}$ . The particles were mounted at the lower end of a J-shaped steel hook with the upper end of the hook fastened to the microbalance (Fig. 4.1). A glass cup (inner diameter 65.7 mm, height 37.9 mm) was filled with deionized water (electrical conductivity of  $5.5 \mu\text{S/m}$ , surface tension  $72.1 \text{ mN/m}$ ) and placed into the temperature jacket of the tensiometer (kept at  $23^\circ\text{C}$ ). The cup of water denoting the air-water interface is slowly moved upwards at a rate of  $6 \text{ mm/min}$  to simulate an upward moving air-water interface over the particle. Particulars of the measurement process are described elsewhere [Chatterjee *et al.*, 2012].

### 4.4.2 Particles

For the purpose of comparison we used two natural sediment particles. The particles were obtained from the Hanford formation at the U.S. Department of Energy's Hanford Nuclear Reservation in south-central Washington. The sediments were collected at a depth of 20 m depth below the surface from a trench face at Hanford. The particles were selected by sieving through meshes with nominal sizes in the range 1 to 2 mm. We placed some of these sediment particles in a petri-dish under a dissection scope and picked individual particles using tweezers. Two particles representing the typical mineralogy of the Hanford formation, a basalt and a clear quartz particle, were selected for the studies. The images of the particles are shown in Fig. 4.2.

### 4.4.3 Surface Characterization by Electron Microscopy

After the determination of the force-position curves, the particles were detached from the J-shaped hook, and coated with platinum-palladium to a thickness of 3 nm under a sputter coater (Model 108auto, Cressington Scientific, Watford, England). The maximum dimensions of the particles were measured under a scanning electron microscope (SEM) equipped with a field-emission gun (Model FEI Quanta 200F, Fei Co., Hillsboro, OR). The SEM was previously calibrated using a standard grid. The dimensions of the particles are listed in Table 4.1.

The particles were mounted on a right-angled block mount under the electron gun at a working distance between 15 mm to 20 mm. The absolute magnification of the imaged particle was kept constant at  $30\times$  for the basalt particle and  $38\times$  for the quartz particle. The magnification level was chosen to get the best possible detail while keeping the whole particle within the SEM view-port. The SEM's

external stage rotation controls were used to rotate the right angle mount by  $5^\circ$  from an initial  $0^\circ$  to  $355^\circ$ , in  $45^\circ$  segments, and SEM images were captured and stored as Tagged Image File Format (TIFF) images using the SEM's imaging software. This allowed us to image the particles' surface at every  $5^\circ$  with rotation occurring around the particles' length ( $x$ -axis).

#### 4.4.4 SEM Image Processing

The saved TIFF images were used to generate single pixel outlines of the particles at angular positions of every  $5^\circ$  after removing the background using Adobe Photoshop CS6. The single pixel outlines at different angles (72 outlines for each particle) were saved as 2-bit (black=0, white=1) TIFF images using IrfanView 4.35 (Irfan Skiljjan, 2012).

### 4.5 Data Analysis

#### 4.5.1 Point-Cloud Generation

The 2-bit TIFF outline files were loaded as matrices with MatLab (8.1, 2013, MathWorks Inc., Natick, MA) and the outline coordinates extracted as non-zero cells in the image matrix. The coordinates of non-zero cells ( $x, y$  location of outline pixels) were converted to real coordinates by dividing with the correct scaling factor, to obtain the coordinates in millimeters units. The outline points in millimeter units were then transformed by rotation along the  $x$ -axis to give coordinates on the particle surface by a rotational transformation. The transformed coordinates were saved as floating point ( $x, y, z$ ) values in a comma separated values (CSV) text file.

The entire process of converting the 2-bit TIFF image to a CSV file containing surface point coordinates was automated using a short MatLab code. The CSV files from each image were combined to generate a single file, which contains the 3D point cloud representing the surface of the particle. Smaller versions (10% of the total points) of the point clouds were also obtained by sorting the points by their angular positions (first by  $\theta$  then by  $\phi$  with respect to the origin (in the center of the particle) and taking every tenth point.

#### 4.5.2 Surface Reconstruction by Triangulation of Point-Cloud

The 10% point-cloud sets were used in MeshLab (v1.32, 2010, GPL/Consiglio Nazionale delle Ricerche, Italy) to generate triangulated meshes. For surface reconstruction (triangulation), we used the ball-pivot algorithm [Bernardini *et al.*, 1999] to generate the triangles. The pivoting ball diameters of 3%, 5% and 10% of the root-mean-square radius of the particles were used to generate the



triangulated meshes. The ball-pivot algorithm was run with the same parameters (see Table 4.2) for each ball diameter. The triangulation algorithm was run until no more faces could be added. Subsequently, the mesh was cleaned up by removing the following: (1) unreferenced vertices, (2) non-manifold vertices, edges and faces, (3) filling up remaining holes using the same ball pivot algorithm parameters, until all holes were filled. The complete process of mesh generation and refining required between 4 to 13 runs of the ball-pivot algorithm on the initial 10% point cloud and the intermediate partially cleaned-up meshes. Fig. 4.3 shows a schematic of the steps from SEM imaging to triangulated mesh reconstruction. Table 4.2 lists the parameters used to calculate the triangulation meshes and results from the surface reconstruction (mesh generation) process. Fig. 4.4 shows the six final meshes (at three resolutions for each particle) obtained after running the ball pivot algorithm on the 10% point clouds generated using outlines from the SEM micrographs. Meshlab was also used to compute face (triangle) normals for every face in all six generated meshes. The meshes generated by Meshlab were saved as standard ASCII mode Stanford Polygon Files (\*.PLY).

### 4.5.3 Theoretical Reconstruction of Force Position Curves

The capillary rise for each of the two particles was calculated using Equation 4.1 with the appropriate values of  $\theta$ ,  $\gamma$  and  $\rho$ . The perimeter of the cross-section of intersection of the particle and a plane normal to the  $z$ -axis, denoting the air-water interface is calculated using a Python program. The program loads a triangulated mesh saved as a PLY file and outputs the perimeter, cross-sectional area and slice volume below a specified plane parallel to the  $xy$ -plane for a particular input mesh. The code also outputs the same parameters (area and perimeter of polygon of cross-section and slice volume) for multiple ( $nZ$ )  $z$ -values within a range, specified by a minimum ( $zLo$ ) and a maximum ( $zHi$ ) value. The variation of polygons of intersection and immersed mesh volume due to intersection between a mesh (particle) and a plane (air-water interface) is depicted in Fig. 4.5.

The output from the Python code generated a text CSV file which lists the  $z$ -value, the area, ( $A$ ), the perimeter, ( $l$ ), and the slice volume, ( $V_{i,z}$ ), of the polygon of intersection. The  $z$ -axis increment,  $((zHi - zLo)/nZ)$ , was used as slice thickness. The CSV files with intersection data were loaded in Microsoft Excel, and the slice volumes cumulatively summed to calculate the immersed volume ( $V_i$ ) of the mesh below each  $z$ -value. The calculated  $l$ ,  $A$ , and  $V_i$  values were used with the appropriate surface tension ( $\gamma$ ), density ( $\rho$ ), and capillary rise ( $h$ ) values, in Equation 4.2, to calculate the total force on the particle due to the moving air-water interface at different positions of the moving interface. The theoretically calculated total force (capillary and buoyancy) was then plotted against the position ( $z$ ), using Origin (v8.6.SR3, 2011, OriginLab Corp., Northampton, MA).

## 4.6 Results and Discussion

### 4.6.1 Analysis and Interpretation of Force-Position Curves

The force-position curves for the basalt and the quartz particles, measured experimentally and calculated from theory for the three different mesh resolutions (3%, 5% and 10%) are plotted in Fig. 4.6, and the maximum capillary forces (negative values) are listed in Table 4.2. The results indicate that, in general, a higher resolution mesh, i.e., using a smaller pivoting ball radius to achieve the triangulation, improves the estimate of the maximum capillary force calculated from theory. In the following sections we discuss Fig. 4.6 in detail.

### 4.6.2 Comparison of Experimental and Theoretical Capillary Forces

The theoretical results do not give a good indication of the increased interaction length in  $z$ -direction of the air-water interface with the sediment particles. This causes a discrepancy observed in the plots, namely, a considerable difference in the position coordinates of the experimental and theoretical force-position curves. The experimental force-position curve differs from the theoretically calculated curves in two key ways: (1) the slope of the experimental force-position curve is less than the theoretically calculated curves, (2) the general size of capillary force ‘features’, i.e., magnitude of abrupt changes in capillary forces, are smaller on the experimental curves than on the theoretical curves.

The difference in slope is directly related to the increase in interaction length (in  $z$  direction) due to interfacial pinning on the roughness features on the particle surface. In other words, the experimental measurements show a smaller value of  $\Delta f/\Delta z$  as compared with the theoretically calculated values. The theoretically calculated force-position curve from the 5% mesh, scaled to experimental curve coordinates (thick dash-dot plot) has a slope very similar to the experimental curve, supporting the presumption that the slope deviation is due to the absence of pinning in the theoretically calculated curves.

The generally smoother and more rounded shape of the experimental curve is due to the phenomena of ‘creeping’ of the interface around roughness features, which occurs when the size of the roughness is comparable to the magnitude of the capillary rise. The experimental curves show a clear discontinuity only when the roughness feature is significantly larger than the capillary rise dimensions leading to a pronounced pinning of the interface, followed by subsequent snap-off. The discontinuities (or ‘features’) on the theoretical curves, on the other hand, are solely due to visible changes in the magnitude of the calculated capillary forces, due to a discernible change in the cross-section of the particle interacting with the air-water interface, e.g., a tapering end of a sediment particle would cause the cross-section to change rapidly. The theoretical calculations, that were used here, do not take into consideration the pinning effect, which

requires that the capillary forces be calculated theoretically by using the Gibbs' inequality condition (Equation 4.3); hence, the theoretical force-position curves do not predict the local interface pinning and snap-off correctly.

## 4.7 Implications

The capillary forces on particles due to moving air-water interfaces, measured experimentally or calculated theoretically can be scaled to particles of colloidal dimensions [Aramrak *et al.*, 2011; Chatterjee *et al.*, 2012; Ally *et al.*, 2012]. Methods of obtaining particle outlines using scanning electron microscopy can be done on micrometer or nanometer-sized particles under high magnification. Alternative methods like atomic force microscopy and three-dimensional laser scanning can be used to generate point clouds for smaller particles, like colloids. At colloidal scales, gravitational and DLVO (electrostatic) forces become less important than capillary forces [Scheludko *et al.*, 1976; Preuss and Butt, 1998a; Shang *et al.*, 2008; Aramrak *et al.*, 2011].

The comparison of experimental and theoretical force-position curves on reconstructed meshes indicates that the higher the resolution of the surface reconstruction, the better is the theoretically predicted maximum capillary force. Our results show that increasing the mesh resolution and accuracy of the point cloud used for the surface reconstruction improves the prediction of the maximum forces. However, the quality of the point cloud data used in this study did not allow for higher resolution ( $<3\%$  pivoting-ball diameter) meshes. Another important consideration is the number of computational runs required to get a complete, closed mesh.

Even though the shape of the force-position curves were better predicted by this method than when we assume particles to be of regular geometric shapes, the theoretical force-position curves that were obtained failed to give an indication of the local pinning, distortion, and snap-off of the interface which is observed in experiments. This limitation reduces the usefulness of the current method to predict residence time of a moving air-water interface in a porous media with colloidal particles, which are useful if pore-scale infiltration rates or diffusion kinetics are being studied in porous media. However, the maximum experimental capillary forces are predicted to reasonable accuracy (within  $\approx 10\%$ ), which indicates that this method will be useful in theoretically predicting attachment or detachment for colloidal particles from porous substrates due to air-water interface movements.

## 4.8 Tables and Figures

Table 4.1: Particle dimensions and contact angles

particle	Maximum dimensions (mm)			$r_{rms}$ (mm)	contact angle ( $^{\circ}$ )
	length	breadth	height		
basalt	3.84	2.68	1.96	5.07	$67 \pm 3$
quartz	3.08	2.17	2.58	4.57	$75 \pm 2$

Table 4.2: Mesh generation (triangulation) using the Ball Pivot (BP) Algorithm. (Top: input parameters; bottom: results.)

basalt		quartz	
<i>Input and Run-time Parameters</i>			
Points in 10% cloud	14642	17331	
Ball diameter <sup>†</sup>	3% 5% 10%	3% 5% 10%	
Ball diameter (mm)	0.152 0.253 0.507	0.137 0.228 0.457	
Clustering radius ( $\mu\text{m}$ )	30.4 50.7 101.3	27.4 45.7 91.3	
Angle threshold* ( $^{\circ}$ )	90		
Runs to convergence <sup>‡</sup>	6 2 1 2 2 1		
<i>Results</i>			
<i>Mesh Generation</i>			
Used vertices	3431 2085 848	3795 2355	999
Faces	6858 4166 1692	7586 4706	1994
Surface area ( $\text{mm}^2$ )	24.704 23.960 23.419	20.033 19.781	19.602
Volume ( $\text{mm}^3$ )	7.224 7.447 7.715	6.366 6.466	6.621
<i>Force-Position Curves (forces in <math>\mu\text{N}</math>)</i>			
Max. Experimental ( $f_{\text{max}}$ )	-636	-493	
Max. Theoretical	-708	-729 -755	-633 -648
Snap-off ( $\Delta f_{\text{snap-off}}$ )	537	357	

<sup>†</sup> Pivoting ball diameter used in mesh generation expressed as a % of the root mean square radius ( $r_{rms}$ ) listed in Table 4.1 above. \* The threshold angle between edges of generated triangles added as faces to the mesh. <sup>‡</sup> The number of runs of the BP Algorithm required to reach a constant number of faces, prior to cleaning for unreferenced vertices, and non-manifold vertices, edges, and faces.

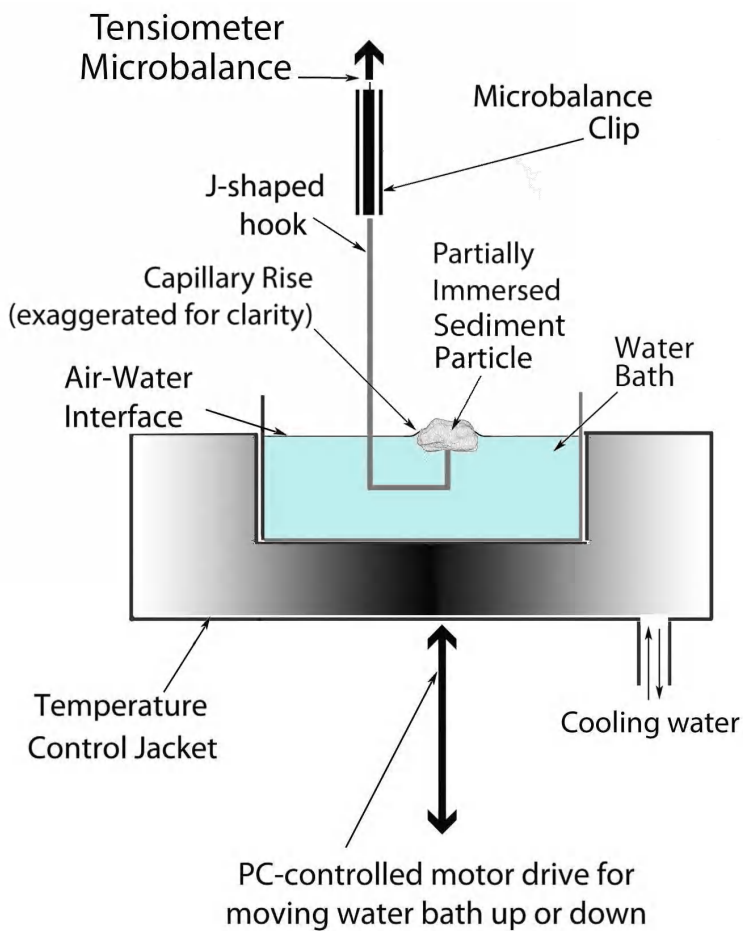


Figure 4.1: Schematic of the experimental setup to measure force-position curves using a microbalance tensiometer in it's measurement position with particle and hook, both partially immersed in water, and interacting with the air-water interface.

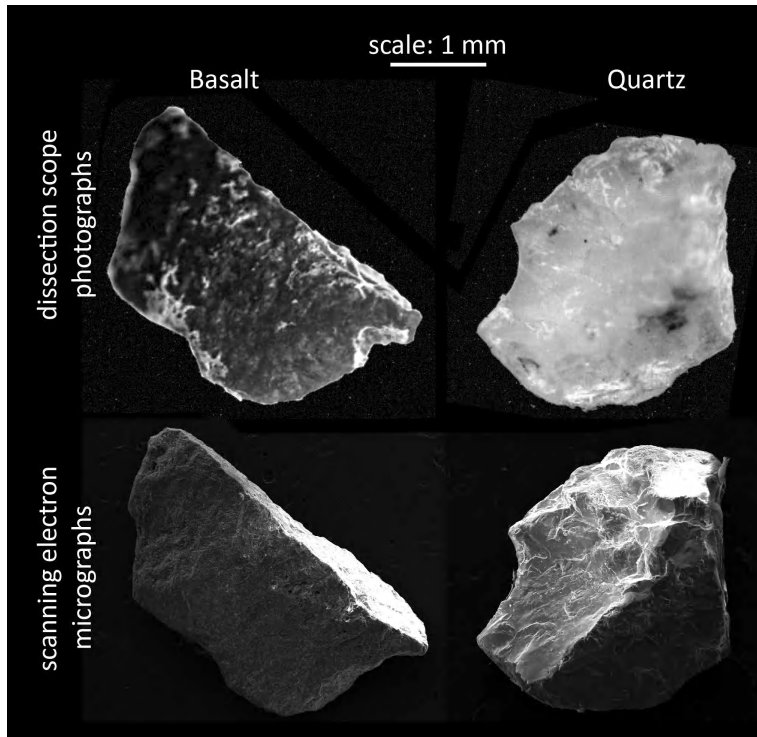


Figure 4.2: Dissection scope (top) and scanning electron microscope (bottom) images of a basalt (left) and a quartz (right) sediment particle.

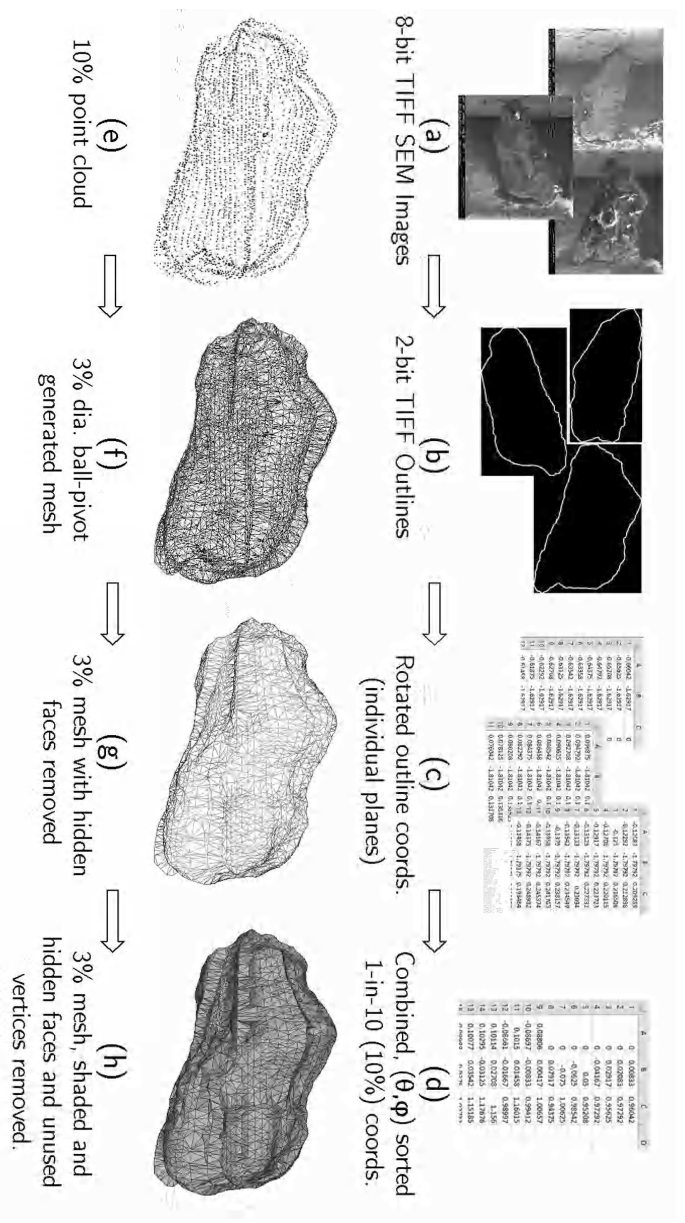


Figure 4.3: Schematic of calculating contact line lengths at the three-phase interfaces (particle surface-air-water) at different ( $z$ -axis) positions of a moving air-water interface. The moving air-water interface ( $xy$ -plane) intersects at different  $z$ -axis positions with a SEM reconstructed surface of a basalt sediment particle.



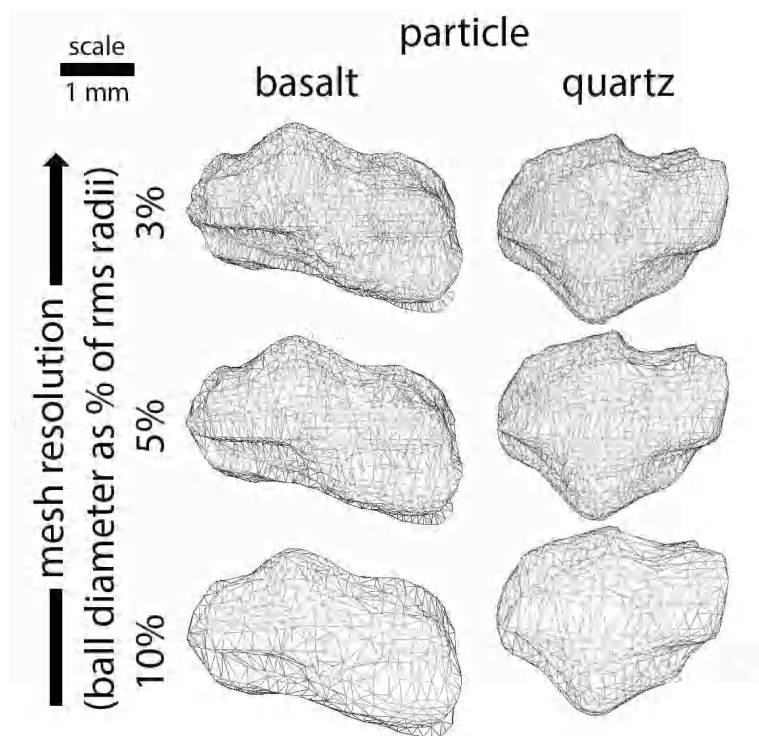


Figure 4.4: Comparison of reconstructed surfaces for natural sediment particles (basalt and quartz). The triangulation used the ball-pivot algorithm to generate the meshes. The size of the pivoting ball diameter is denoted as a percentage of the rms radius of the particle.

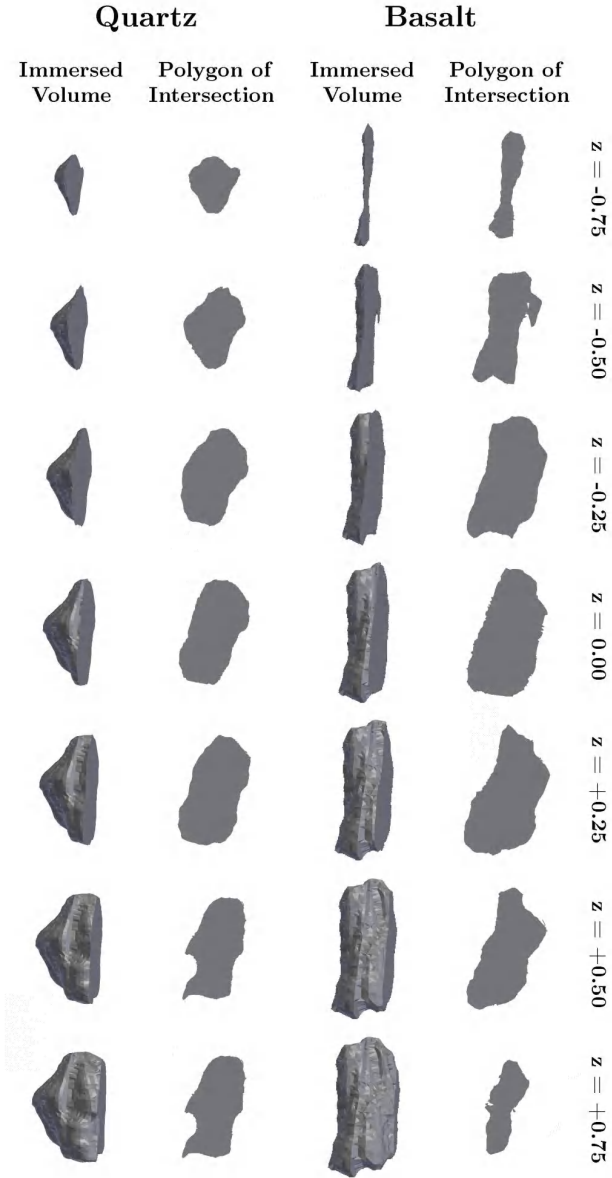


Figure 4.5: Variation of the polygon of intersection and the immersed mesh volume when a moving plane (moving air-water interface) intersects with a mesh (sediment particle surface) at different positions of the air-water interface. The meshes used are the 3% meshes.

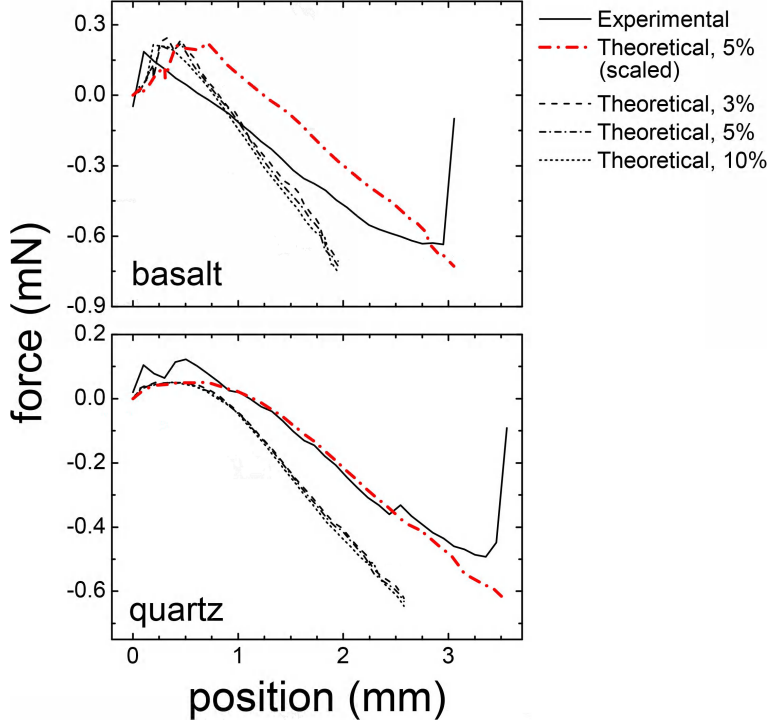


Figure 4.6: Comparison of reconstructed force-position curves for immersion of natural sediment particles (basalt and quartz) at an air-water interface. The solid line denotes the experimentally measured force-position curve. The dashed black lines denote the theoretically reconstructed force-position curves for different resolutions of the surface reconstruction meshes. The dash-dot red line denotes the theoretically reconstructed force-position curve for a mesh reconstruction using a ball diameter 5% of the particle rms radius, normalized over the total interaction distance of the experimental force-position curve.



# Chapter 5

## Summary and Conclusions

In Chapters 2–4, the capillary forces on sub-surface particles are described with the objective to quantify the forces due to moving air-water interfaces. Even though the focus of the studies was on particles in the millimeter-scale, the forces calculated are known to scale proportionally to smaller sized particles like micron sized colloids and nanoparticles. In view of this fact, the results from these studies can be used in understanding the magnitude of the capillary forces acting on colloids in media where moving air-water interfaces constitute an important component. Such capillary forces on particles have been implicated in colloid mediated transport of contaminants and nutrients in the soil subsurface. Estimating the magnitude of capillary forces becomes increasingly important as particle size reduces because other forces like gravitational and DLVO (electrostatic) forces become less important.

### 5.1 Calculating Capillary Forces on Sediment Particles Shaped as Spheres, Ellipsoids and Cylinders.

Experimental capillary forces on natural sediment particles were measured and compared with capillary forces on control particles made of synthetic hydrophobic material (PTFE) of standard shapes. The effect of organic coatings on natural sediments were also measured to understand the effect of such coatings on the capillary forces experienced by such particles in the natural environment. Seven different mineral particles were used in this study. The different mineral has different contact angles with an air-water interface. We also estimated the capillary forces on the natural particles from theoretical first principles, assuming the particles to be of standard shapes. The natural sediment particles were assumed to be of spherical, cylindrical and ellipsoidal shapes. The dimensions of the assumed shapes were obtained in two ways: (1) from experimentally measured maximum

dimensions to obtain an “encompassing” shape, and (2) as volume equivalent shapes with volumes obtained from buoyancy measurements and relative axial dimensions obtained from root-mean-square axial dimensions.

The results showed that natural organic coatings made only minor difference in the magnitude of capillary forces on the sediment particles. The theoretical calculations of capillary forces assuming geometric shapes showed that assuming the particles to be volume-equivalent ellipsoids gave the best estimate of the maximum capillary forces and of the shape of the force-position curve of a sediment particle interacting with a moving air-water interface. Assuming sediment particles, to be spheres and cylinders in theoretical calculations, consistently underestimated and overestimated the capillary forces, respectively.

## 5.2 Capillary Forces on 3D Printed Particles of Standard Geometric Shapes.

The objective of this study was to study how overall particle shapes and distinctive features of various geometric shapes affect the shape of the force-position curves generated when a moving air-water interface interacts with a mm-scale particle. We investigated capillary forces on particles fabricated using a 3D printer. We measured the maximum capillary forces measured using an experimental setup and then evaluated the efficacy of theoretical methods to reconstruct the experimental force-position curves and calculate the maximum capillary forces experienced by these particles.

Our results showed that for rounded particles, the theoretical calculations gave a closer estimate of the force-position curve for the ellipsoidal particles, whereas the maximum capillary forces were underestimated for the spherical particle. The theoretical reconstruction also failed to predict the final snap-off of the interface from the top of the particles. For particles with a fixed cross-section, the force position curves were found to have a typical three-segment form. The first and last segments are characteristic of an interface getting increasingly distorted after getting pinned to a edge on the particle. We reconstructed this overall three-segment shape of the experimental force-position curves from theoretical calculations assuming the Gibbs’ inequality condition.

However, the theoretical reconstruction could not describe the rounding of the force-position curve between the segments that is observed in the experimental force-position curve for particles with a fixed cross-section. This rounding between segments is explained by a slow “creeping” of the air-water interface over the edge of the particle, which results in a more gradual change of the capillary forces rather than the abrupt change expected from theory. The interface “creeping” phenomena was also observed for particles with a tapering cross-section where the air-water interface was creeping across the hard edge at the bottom of the particle. The gradual vanishing of the capillary force with a

remnant buoyancy force was correctly predicted by the theoretical calculations from particles with a tapering cross-section.

However, in all three categories of particles there were discrepancies in the magnitudes of the maximum capillary forces predicted by theory and the experimentally observed ones. This is explained by the roughness of the of the 3D printed particles' surfaces which causes local pinning and snap-off of the moving interface all along the direction of movement of the interface. This local pinning phenomena cause the deviation of the shape of the force-position curve from the ideal shape predicted by theoretical calculations.

## 5.3 Numerical Reconstruction of Surfaces and Force-Position Curves of Natural Sediment Particles.

In this chapter we describe the reconstruction of the rough surface of sediment particles using scanning electron microscopy and then subsequently performed capillary force calculations on the reconstructed surfaces due to a 'theoretical' moving air-water interface. The resulting calculated capillary forces were plotted against the position of the interface and the theoretical force-position curves were compared with experimentally obtained force-position curves. This surface and force-position curve reconstruction process was done for two different sediment particles, at three different resolution of surface reconstruction. The theoretically calculated maximum capillary forces that were predicted were within  $\approx 10\%$  of the maximum capillary forces measured in experiments. The general shapes of the force-position curves are also correctly predicted.

However, the theoretical surface and subsequent force-position curve reconstruction process is computationally intensive. Also, the theoretical calculation methods could neither predict the position locations of the major snap-off features of the experimental curve nor its extending due to pinning, because the we did not consider the formation of non-equilibrium contact angles (Gibbs inequality condition). However, overall, this is a good method to predict shapes of force-position curve, and get a value of the maximum capillary forces within reasonable accuracy.

## 5.4 Conclusion

The studies described above predict force-position curves of different meso-scale particles when interacting with a moving air-water interface, a situation frequently found when water infiltration or drainage occurs through a porous medium like soils. In general, these methods give a much closer estimate of the real capillary forces acting on irregularly shaped particles, which are found in natural

systems. The methods are also easily scaled to smaller particle like colloids. This allows us to use such methods to find the capillary forces responsible for transport of colloids in unsaturated, porous media due to water movement. Such forces are of importance in studies involving contaminant and nutrient transport, the chemical kinetics and physical diffusion studies of pollutants and pathogens and in general understanding of systems where multiphase transport occurs.



# Bibliography

- Ally, J., M. Kappl, and H.-J. Butt, Adhesion of particles with sharp edges to air-liquid interfaces, *Langmuir*, 28, 11042–11047, 2012.
- Aramrak, S., M. Flury, and J. B. Harsh, Detachment of deposited colloids by advancing and receding air-water interfaces, *Langmuir*, 27, 9985–9993, 2011.
- Aramrak, S., M. Flury, J. B. Harsh, R. L. Zollars, and H. P. Davis, Does colloid shape affect detachment of colloids by a moving air–water interface?, *Langmuir*, 29, 5770–5780, 2013.
- Bernardini, F., J. Mittleman, H. Rushmeier, C. Silva, and G. Taubin, The ball-pivoting algorithm for surface reconstruction, *IEEE Transactions on Visualization and Computer Graphics*, 5, 349–359, 1999.
- Brown, A. B. D., C. G. Smith, and A. R. Rennie, Fabricating colloidal particles with photolithography and their interactions at an air-water interface, *Phys. Rev. E*, 62, 951–960, 2000.
- Chatterjee, N., and M. Flury, Effect of particle shape on capillary forces at an air-water interface, *Langmuir*, 2013.
- Chatterjee, N., S. Lapin, and M. Flury, Capillary forces between sediment particles and an air-water interface, *Environ. Sci. Technol.*, 46, 4411–4418, 2012.
- Cheng, T., and J. E. Saiers, Mobilization and transport of in situ colloids during drainage and imbibition of partially saturated sediments, *Water Resour. Res.*, 45, W08414, doi: 10.1029/2008WR007494, 2009.
- Crist, J. T., J. F. McCarthy, Y. Zevi, P. C. Baveye, J. A. Troop, and T. S. Steenhuis, Pore-scale visualization of colloid transport and retention in partially saturated porous media, *Vadose Zone J.*, 3, 444–450, 2004.
- Crist, J. T., Y. Zevi, J. F. McCarthy, J. A. Troop, and T. S. Steenhuis, Transport and retention mechanisms of colloids in partially saturated porous media, *Vadose Zone J.*, 4, 184–195, 2005.

- Danov, K. D., and P. A. Kralchevsky, Capillary forces between particles at a liquid interface: General theoretical approach and interactions between capillary multipoles, *Adv. Colloid. Interface Sci.*, *154*, 91–103, 2010.
- Danov, K. D., P. A. Kralchevsky, B. N. Naydenov, and G. Brenn, Interactions between particles with an undulated contact line at a fluid interface: Capillary multipoles of arbitrary order, *J. Colloid Interface Sci.*, *287*, 121–134, 2005.
- de Gennes, P.-G., F. Brochard-Wyart, and D. Quéré, *Capillarity and Wetting Phenomena. Drops, Bubbles, Pearls, Waves*, Springer, New York, 2004.
- Ecke, S., M. Preuss, and H. J. Butt, Microsphere tensiometry to measure advancing and receding contact angles on individual particles, *J. Adhesion Sci. Technol.*, *13*, 1181–1191, 1999.
- Englert, A., M. Krasowska, D. Fornasiero, J. Ralston, and J. Rubio, Interaction force between an air bubble and a hydrophilic spherical particle in water, measured by the colloid probe technique, *Int. J. Mineral Processing*, *92*, 121–127, 2009.
- Flury, M., and H. Qiu, Modeling colloid-facilitated contaminant transport in the vadose zone, *Vadose Zone J.*, *7*, 682–697, 2008.
- Flury, M., J. B. Mathison, and J. B. Harsh, *In situ* mobilization of colloids and transport of cesium in Hanford sediments, *Environ. Sci. Technol.*, *36*, 5335–5341, 2002.
- Fournier, J.-B., and P. Galatola, Anisotropic capillary interactions and jamming of colloidal particles trapped at a liquid-fluid interface, *Phys. Rev. E*, *65*, 031601, 2002.
- Gao, B., J. E. Saiers, and J. N. Ryan, Deposition and mobilization of clay colloids in unsaturated porous media, *Water Resour. Res.*, *40*, W08602, doi:10.1029/2004WR003189, 2004.
- Gao, B., T. S. Steenhuis, Y. Zevi, V. L. Morales, J. L. Nieber, B. K. Richards, J. F. McCarthy, and J.-Y. Parlange, Capillary retention of colloids in unsaturated porous media, *Water Resour. Res.*, *44*, W04504, doi:10.1029/2006WR005332, 2008.
- Gillies, G., M. Kappl, and H. Butt, Direct measurements of particle-bubble interactions, *Adv. Colloid Interface Sci.*, *114*, 165–172, 2005.
- Gomez-Suarez, C., J. Noordmans, H. C. van der Mei, and H. J. Busscher, Detachment of colloidal particles from collector surfaces with different electrostatic charge and hydrophobicity by attachment to air bubbles in a parallel plate flow chamber, *Phys. Chem. Chem. Phys.*, *1*, 4423–4427, 1999a.

- Gomez-Suarez, C., J. Noordmans, H. C. van der Mei, and H. J. Busscher, Removal of colloidal particles from quartz collector surfaces as simulated by the passage of liquid-air interfaces, *Langmuir*, *15*, 5123–5127, 1999b.
- Grolimund, D., M. Borkovec, K. Barmettler, and H. Sticher, Colloid-facilitated transport of strongly sorbing contaminants in natural porous media: a laboratory column study, *Environ. Sci. Technol.*, *30*, 3118–3123, 1996.
- Gunde, R., S. Hartland, and R. Mader, Sphere tensiometry: a new approach to simultaneous and independent determination of surface tension and contact angle, *J. Colloid Interface Sci.*, *176*, 17–30, 1995.
- Hesla, T. I., and D. D. Joseph, The maximum contact angle at the rim of a heavy floating disk, *J. Colloid Interface Sci.*, *279*, 186–191, 2004.
- Jacobsen, O. H., P. Moldrup, H. de Jonge, and L. W. de Jonge, Mobilization and transport of natural colloids in a macroporous soil, *Phys. Chem. Earth.*, *23*, 159–162, 1998.
- Karathanasis, A. D., Subsurface migration of copper and zinc mediated by soil colloids, *Soil Sci. Soc. Am. J.*, *63*, 830–838, 1999.
- Keller, A. A., and M. Auset, A review of visualization techniques of biocolloid transport processes at the pore scale under saturated and unsaturated conditions, *Adv. Water Resour.*, *30*, 1392–1407, 2007.
- Kralchevsky, P. A., N. D. Denkov, and K. D. Danov, Particles with an undulated contact line at a fluid interface: Interaction between capillary quadrupoles and rheology of particulate monolayers, *Langmuir*, *17*, 7694–7705, 2001.
- Kretzschmar, R., M. Borkovec, D. Grolimund, and M. Elimelech, Mobile subsurface colloids and their role in contaminant transport, *Adv. Agron.*, *66*, 121–193, 1999.
- Lazouskaya, V., L.-P. Wang, H. Gao, X. Shi, K. Czymmek, and Y. Jin, Pore-scale investigation of colloid retention and mobilization in the presence of a moving air-water interface, *Vadose Zone J.*, *10*, 1250–1260, 2011.
- Leenaars, A. F. M., and S. B. G. O’Brien, Particle removal from silicon substrates using surface tension forces, *Philips J. Res.*, *44*, 183–209, 1989.
- Lehle, H., and M. Oettel, Importance of boundary conditions for fluctuation-induced forces between colloids at interfaces, *Phys. Rev. E*, *75*, 011602, 2007.
- Lehle, H., E. Noruzifar, and M. Oettel, Ellipsoidal particles at fluid interfaces, *Eur. Phys. J. E: Soft Matter Biol. Phys.*, *26*, 151–160, 2008.

- Levin, J. M., J. S. Herman, G. M. Hornberger, and J. E. Saiers, Colloid mobilization from a variably saturated, intact soil core, *Vadose Zone J.*, 5, 564–569, 2006.
- Lewandowski, E. P., J. A. Bernate, P. C. Searson, and K. J. Stebe, Rotation and alignment of anisotropic particles on nonplanar interfaces, *Langmuir*, 24, 9302–9307, 2008.
- Loudet, J. C., A. G. Yodh, and B. Pouligny, Wetting and contact lines of micrometer-sized ellipsoids, *Phys. Rev. Lett.*, 97, 018304, 2006.
- Loudet, J. C., A. M. Alsayed, J. Zhang, and A. G. Yodh, Capillary interactions between anisotropic colloidal particles, *Phys. Rev. Lett.*, 94, 018301, 2005.
- McCarthy, J. F., and J. M. Zachara, Subsurface transport of contaminants, *Environ. Sci. Technol.*, 23, 496–502, 1989.
- McCarthy, J. F., and L. D. McKay, Colloid transport in the subsurface: Past, present, and future challenges, *Vadose Zone J.*, 3, 326–337, 2004.
- Morris, G., M. Pursell, S. Neethling, and J. Cilliers, The effect of particle hydrophobicity, separation distance and packing patterns on the stability of a thin film, *J. Colloid Interface Sci.*, 327, 138–144, 2008.
- Morris, G., S. Neethling, and J. Cilliers, The effects of hydrophobicity and orientation of cubic particles on the stability of thin films, *Miner. Eng.*, 23, 979–984, 2010, Froth Flotation.
- Morris, G., S. Neethling, and J. Cilliers, A model for investigating the behaviour of non-spherical particles at interfaces, *J. Colloid Interface Sci.*, 354, 380–385, 2011.
- Noordmans, J., P. J. Wit, H. C. van der Mei, and H. J. Busscher, Detachment of polystyrene particles from collector surfaces by surface tension forces induced by air-bubble passage through a parallel plate flow chamber, *J. Adhesion Sci. Technol.*, 11, 957–969, 1997.
- Preuss, M., and H. Butt, Direct measurement of particle-bubble interactions in aqueous electrolyte: dependence on surfactant, *Langmuir*, 14, 3164–3174, 1998a.
- Preuss, M., and H. J. Butt, Measuring the contact angle of individual colloidal particles, *J. Colloid Interface Sci.*, 208, 468–477, 1998b.
- Princen, H. M., Equilibrium shape of interfaces, drops, and bubbles. Rigid and deformable particles at interfaces, *Surface Colloid Sci.*, 2, 1–84, 1969.

- Ryan, J. N., T. H. Illangasekare, M. I. Litaor, and R. Shannon, Particle and plutonium mobilization in macroporous soils during rainfall simulations, *Environ. Sci. Technol.*, **32**, 476–482, 1998.
- Saers, J. E., and J. J. Lenhart, Colloid mobilization and transport within unsaturated porous media under transient-flow conditions, *Water Resour. Res.*, **39**, 1019, doi:10.1029/2002WR001370, 2003.
- Saers, J. E., G. M. Hornberger, D. B. Grower, and J. S. Herman, The role of moving air-water interfaces in colloid mobilization within the vadose zone, *Geophys. Res. Lett.*, **30**, 2083, doi:10.1029/2003GL018418, 2003.
- Scheludko, A., B. V. Toshev, and D. T. Bojadjev, Attachment of particles to a liquid surface (Capillary theory of flotation), *J. Chem. Soc. Faraday Trans. I*, **72**, 2815–2828, 1976.
- Shang, J., M. Flury, and Y. Deng, Force measurements between particles and the air-water interface: Implications for particle mobilization in unsaturated porous media, *Water Resour. Res.*, **45**, W06420, doi:10.1029/2008WR007384, 2009.
- Shang, J., M. Flury, G. Chen, and J. Zhuang, Impact of flow rate, water content, and capillary forces on *in situ* colloid mobilization during infiltration in unsaturated sediments, *Water Resour. Res.*, **44**, W06411, doi:10.1029/2007WR006516, 2008.
- Sharma, P., H. Abdou, and M. Flury, Effect of the lower boundary condition and flotation on colloid mobilization in unsaturated sandy sediments, *Vadose Zone J.*, **7**, 930–940, 2008a.
- Sharma, P., M. Flury, and J. Zhou, Detachment of colloids from a solid surface by a moving air-water interface, *J. Colloid Interface Sci.*, **326**, 143–150, 2008b.
- Singh, P., and D. D. Joseph, Fluid dynamics of floating particles, *J. Fluid Mech.*, **530**, 31–80, 2005.
- Stamou, D., C. Duschl, and D. Johannsmann, Long-range attraction between colloidal spheres at the air-water interface: The consequence of an irregular meniscus, *Phys. Rev. E*, **62**, 5263–5272, 2000.
- Tee, G. J., *Surface area and capacity of ellipsoids in n dimensions*, Technical report, Department of Mathematics, University of Auckland, Auckland, New Zealand, 2004.
- van Nierop, E. A., M. A. Stijnman, and S. Hilgenfeldt, Shape-induced capillary interactions of colloidal particles, *Europhys. Lett.*, **72**, 671–677, 2005.

- Veerapaneni, S., J. Wan, and T. Tokunaga, Motion of particles in film flow, *Environ. Sci. Technol.*, *34*, 2465–2471, 2000.
- Wan, J. M., and T. K. Tokunaga, Film straining of colloids in unsaturated porous media: conceptual model and experimental testing, *Environ. Sci. Technol.*, *31*, 2413–2420, 1997.
- Wan, J. M., J. L. Wilson, and T. L. Kieft, Influence of the gas-water interface on transport of microorganisms through unsaturated porous media, *Appl. Environ. Microbiol.*, *60*, 509–516, 1994.
- Yamamoto, T., Y. Harada, K. Fukui, and H. Yoshida, AFM investigation of the surface properties of silica particles dispersed by bead milling, *Colloids Surf., A*, *362*, 97–101, 2010.
- Zevi, Y., A. Dathe, J. F. McCarthy, B. K. Richards, and T. S. Steenhuis, Distribution of colloid particles onto interfaces in partially saturated sand, *Environ. Sci. Technol.*, *39*, 7055–7064, 2005.
- Zhang, L., L. Ren, and S. Hartland, More convenient and suitable methods for sphere tensiometry, *J. Colloid Interface Sci.*, *180*, 493–503, 1996.
- Zhang, L., L. Ren, and S. Hartland, Detailed analysis of determination of contact angle using sphere tensiometry, *J. Colloid Interface Sci.*, *192*, 306–318, 1997.
- Zhang, P., W. P. Johnson, and R. Rowland, Bacterial tracking using ferrographic separation, *Environ. Sci. Technol.*, *33*, 2456–2460, 1999.
- Zhuang, J., J. F. McCarthy, J. S. Tyner, E. Perfect, and M. Flury, In-situ colloid mobilization in Hanford sediments under unsaturated transient flow conditions: Effect of irrigation pattern, *Environ. Sci. Technol.*, *41*, 3199–3204, 2007.











*Department of Crop & Soil Sciences*

© WASHINGTON STATE UNIVERSITY  
2013